2013

Optimization of Mixing in a Simulated Biomass Bed Reactor with a Center Feeding Tube

Michael T. Blatnik
University of Massachusetts Amherst

OPTIMIZATION OF MIXING IN A SIMULATED BIOMASS BED REACTOR WITH A CENTER FEEDING TUBE

A Thesis Presented

by

MICHAEL T. BLATNIK

Submitted to the Graduate School of the
University of Massachusetts Amherst in partial fulfillment
of the requirements for the degree of

MASTER OF SCIENCE IN MECHANICAL ENGINEERING

September 2013

Mechanical and Industrial Engineering

OPTIMIZATION OF MIXING IN A SIMULATED BIOMASS BED REACTOR WITH A CENTER FEEDING TUBE

A Thesis Presented

by

MICHAEL T. BLATNIK

Approved as to style and content by:

Stephen M. de Bruyn Kops, Chair

David P. Schmidt, Member

T. J. Mountziaris, Member

Donald L. Fisher, Department Chair
Mechanical and Industrial Engineering

ACKNOWLEDGMENTS

This work was funded by the National Science Foundation Office of Emerging Frontiers in Research and Innnovation (EFRI) grant number 0937895 and greatly benefited from discussions with Prof. George Huber.

High performance computing resources were provided by the U.S. Department of Defense High Performance Computing Modernization Program at the Army Research Laboratory (ARL) and at the Army Engineer Research and Development Center (ERDC).

ABSTRACT

OPTIMIZATION OF MIXING IN A SIMULATED BIOMASS BED REACTOR WITH A CENTER FEEDING TUBE

SEPTEMBER 2013

MICHAEL T. BLATNIK

B.Sc., LYNCHBURG COLLEGE

M.S.M.E., UNIVERSITY OF MASSACHUSETTS AMHERST

Directed by: Professor Stephen M. de Bruyn Kops

Producing gasoline-type fuels from lignocellulosic biomass has two advantages over producing alcohol-type fuels from plant sugars: gasoline has superior fuel characteristics and plant lignin/cellulose does not compete with human food supplies. A promising technology for converting lignocellulose to fuel is catalytic fast pyrolysis (CFP). The process involves injecting finely ground biomass into a fluidized bed reactor (FBR) at high temperatures, which reduce the biomass to gases that react inside the catalyst particles. This entails complex hydrodynamics to efficiently mix a stream of biomass into a catalyst bed that is fluidized by a separate stream of inert gas. Understanding the hydrodynamics is complicated by the fact that the entire process occurs inside a heavily insulated, opaque, reactor vessel. Numerical simulations offer a promising approach to understanding, predicting, and optimizing hydrodynamic mixing in a CFP biomass reactor.

The purpose of this research is to understand the simulation techniques and statistical measures appropriate for quantifying mixing in a CFP biomass reactor. The methodology is validated against the canonical configuration of a non-reacting, single-inlet fluidized bed. A new finding is that the minimum bubbling velocity may be predicted by a significant increase in temporal variance of the pressure drop. The methodology is then applied to a non-canonical FBR in which biomass is injected into the catalyst bed via a vertical center tube. Since no hydrodynamic mixing data exist from laboratory experiments, mixing is inferred from the aromatics yield from the laboratory reactor. Flow configurations with which simulations demonstrate the best mixing have the highest aromatic yields in the experiments. The simulations indicate that when the bed is in the bubbling regime, the gasified biomass from the center tube is efficiently mixed radially throughout the catalyst bed. If the flow rate of inert gas is insufficient to bubble the bed, then the gasified biomass exits the center tube, reverses direction, and flows upward along the tube's outside wall. Provided the bed is bubbling due to the inert gas stream, the upper limit on the flow through the center tube, and thus the aromatic yield potential, has yet to be determined.

TABLE OF CONTENTS

LIST OF TABLES

Table **Page**

LIST OF FIGURES

Figure **Page**

LIST OF SYMBOLS

β	Interphase drag coefficient (kg/(m^3·s))
$\boldsymbol{g}$	Gravity constant (m/s^2)
$\boldsymbol{q}_k$	Heat flux of phase k (W/m^2)
$\boldsymbol{v}_k$	Velocity of phase k (cm/s)
$\bar{\bar{\tau}}_k$	Viscous stress tensor of phase k (N/m^2)
δ	Mesh size, uniform in both x and y directions (m)
γ_s	Dissipation of granular energy due to inelastic particle collisions (kg/(m^3·s))
κ_{dil}	Dilute phase granular conductivity (kg/(m·s))
κ_s	Solids thermal conductivity (kg/(m·s))
λ_k	Bulk viscosity of phase k (Pa·s)
μ_g	Gas dynamic viscosity (Pa·s)
μ_s	Solids shear viscosity (Pa·s)
μ_f	Frictional viscosity (Pa·s)
Ω	Bed expansion, percentage above h_{mf} (dimensionless)
Φ	Statistical parameter related to variance of ξ: $\left\langle \overline{\xi'^2} \right\rangle / \left\langle \overline{\xi} \right\rangle^2$ (dimensionless)
ϕ	Angle of internal friction/azimuthal angle coordinate position (rad)
ψ	Statistical parameter related to variance of α_s: $\left\langle \overline{\alpha_s'^2} \right\rangle / \alpha_{s,max}'^2$ (dimensionless)
ρ_k	Density of phase/species k (kg/m^3)
Θ	Granular temperature (m/s^2)
θ	Statistical parameter related to mean of ξ: $\left\langle \overline{\xi(r)} \right\rangle / \xi_{ideal}$ (dimensionless)
ε	Statistical parameter related to mean of α_s: $\left\langle \overline{\alpha_s} \right\rangle / \alpha_{s,max}$ (dimensionless)
α_k	Volume fraction of phase k (dimensionless)
$\alpha_{s,max}$	Maximum solids volume fraction packing limit
$\alpha_{s,min}$	Minimum solids volume fraction for frictional model

ξ	Mixture fraction (dimensionless)
ξ_{ideal}	Ideal mixture fraction in a well-mixed case (dimensionless)
A	Frictional model empirical constant
C_D	Coefficient of drag
D	Bed depth (m)
d_s	Particle diameter (m)
e	Coefficient of restitution
F_v	Viscous drag force (N)
fl	Abbreviation for the bottom fluidizer inlet
Fr	Frictional model empirical constant (Pa)
ft	Abbreviation for the feed tube inlet
g_0	Radial distribution function
H	Reactor height (m)
h	Height of the catalyst bed (cm)
h_k	Specific enthalpy of phase k (J/kg)
H_T	Height of feed tube above bottom fluidizer (cm)
h_{mf}	Bed height at minimum fluidization velocity (dimensionless)
J_s	Dissipation of granular energy due to velocity fluctuations (kg/(m^3·s))
K	Empirical constant (N)
m	Total mass of the catalyst (g)
n	Frictional model empirical constant
O	Arbitrary, cell-centered quantity (dimensionless)
P	Pressure (Pa)
p	Frictional model empirical constant
P_s	Solids pressure (Pa)
P_f	Normal frictional stress (Pa)
Q_{fl}	Fluidizer flow rate (cm^3/s)
Q_{ft}	Feed tube flow rate (cm^3/s)
Q_{total}	Total flow rate $Q_{fl} + Q_{ft}$ (cm^3/s)
R	Radius of the reactor (cm)
r	Radial coordinate (m)
R_T	Radius of the feed tube (cm)

T Temperature (K)

t Time (s)

T_S Sampling period for statistical analysis (s)

u_k x-component of $\boldsymbol{v_k}$ for phase k (cm/s)

$V(r,t)$ Volume occupied by an axial slice of the catalyst bed a radial location r and time t (cm^3)

$V(z)$ Volume occupied by a radial slice of the reactor at a height z (cm^3)

$V_{bed}(t)$ Volume occupied by the catalyst bed at time t (cm^3)

v_{fl} Feed tube velocity (cm/s)

v_{fl} Fluidizer velocity (cm/s)

v_k y-component of $\boldsymbol{v_k}$ for phase k (cm/s)

v_{mf} Minimum fluidization velocity (cm/s)

x Cartesian position coordinate (m)

X_i Mole fraction of species i (dimensionless)

y Cartesian position coordinate (m)

Y_i^{∞} Free-stream mass fraction of species i (dimensionless)

Y_i^{ideal} Ideal, well-mixed mass fraction of species i (dimensionless)

Y_i Mass fraction of species i (dimensionless)

z Axial coordinate (m)

f# Abbreviation for a simulation run with $Q_{ft}/Q_{total} = \#\%$

Re Relative Reynolds number

t# Abbreviation for a simulation run with $Q_{total}/Q_{mf} = \#$

CHAPTER 1

BACKGROUND

The goal of this research is to numerically simulate and statistically quantify the hydrodynamics of a non-standard fluidized bed using catalytic fast pyrolysis (CFP) for the production of gasoline-grade fuel from cellulose. The reactor is under development by the Emerging Frontiers in Research and Innovation (EFRI) group at both the University of Massachusetts Amherst and the University of Wisconsin−Madison. From a downward-facing center feeding tube, cellulose or other wood feedstocks are injected into a fluidized bed partially filled with zeolite (ZSM5) catalyst particles. The process is maintained at high temperatures (773 K), which causes the biomass to pyrolize into oxygenated vapors. As the vapors enter the catalyst pores, they are converted to aromatics, the desired product, as well as olefins, CO, CO_2, water, and other by-products. The aromatics are desirable because they can be converted to a gasoline-range hydrocarbon fuel. Advantages of this emerging technology include short mixing residence times (2−10 s), low cost of the catalyst, an abundance of feedstock, a ready-to-use fuel product, and high oil prices.

Numerical simulations are performed using computational fluid dynamics (CFD) codes in the commercial software ANSYS© Fluent, version 14.0. We neglect chemical reactions since the hydrodynamic mixing is the study of interest. To assess the accuracy of the simulations, we compare our results with data from the laboratory reactor and literature models.

1.1 Fluidized Beds

A typical fluidized bed is a cylinder, containing a bed of particles supported by a bottom plate through which a fluidizing gas is introduced [30]. At sufficient velocities, the gas will suspend or lift the particles, causing them to move throughout the bed. The gas velocity required to support the weight of the bed is called the minimum fluidization velocity v_{mf}. The value is empirically determined by increasing the gas velocity until the pressure change (ΔP) across the height of the bed equals the weight of the bed over the inlet surface area. Momentum losses due to collisions between the particles and the walls or bottom plate cause $\Delta P >$ bed weight/area. The fluctuations are primarily due to the center of mass of the bed accelerating up and down.

After minimum fluidization velocity, increases in gas velocity result in "bubbles," which are voidage regions with low particle density that rise to the top of the bed. The behavior of such fluidization depends upon the properties of the solids and of the gas, the fluidizing velocity, and the geometry of the bed.

1.2 Flow Regimes

Fluidization flow regimes are divided into 4 categories: expanding, bubbling, slugging, and turbulent [30]. The expanding regime has no bubbles. Increases in velocity yield a higher bed height and thus a lower average solids volume fraction within the bed. Bed expansion does not always occur before bubbling but is typical for smaller particles [29].

The bubbling flow regime occurs when the fluidizing velocity rises above v_{mb}, the minimum bubbling velocity. At this point, bubbles begin to form that grow with bed height but typically do not reach full bed width, except in narrow, tall beds. Higher fluidizing velocities generally lead to larger bubbles. A bubbling bed is an essential component of mixing within the bed. In industry, fluidized beds are used to facilitate chemical processes such as coal

gasification, combustion, and biomass conversion. Ideal mixing maximizes the stoichiometric amount of desired products [18].

The slugging flow regime occurs at high fluidizing velocities when bubbles ("slugs") in deep, narrow beds grow to the diameter of the bed. Slug flow can further be divided into axisymmetric slugs, wall slug, plugs, and continuous slug flow [20]. At even higher velocities, the bed can transition from either a bubbling or slugging flow to a turbulent regime. In this scenario, the bubbles or slugs break up into smaller bubbles and the particles form clusters or streamers. At this point, the solids and the gas phase become more indistinguishable and the flow more dilute [20]. Every fluidized bed does not necessarily go through each of these four stages. The uniqueness of fluidization behavior depends upon the particles' properties.

1.3 Geldart Classification of Particles

Geldart classified particles into 4 different categories (Geldart Type A, B, C, and D), depending on the particle's size, density, fine content, and cohesiveness [29]. Particles of the same type tend to progress through the same fluidization regimes.

Type A particles, such as fine catalysts, have small diameters and low densities ($\rho_s < 1400$ kg/m^3). Type A particle beds undergo expansion before bubbling, and thus $v_{mb}/v_{mf} > 1$. In addition, bubble growth is limited to a fixed maximum bubble size [20], which is relevant whether or not slugs can form.

Geldart Type B particles exist within a range of a mean particle diameters ($40 < d_s < 500$ μm) and a range of densities (4000 kg/m^3 $< \rho_s <$ 1400 kg/m^3). For particles of this type, bubbling begins at minimum fluidization velocity, i.e., $v_{mb}/v_{mf} = 1$.

Particles belonging to Type C consist of fine, cohesive powders that are difficult to fluidize. In small-diameter reactors, the particles lift as plugs. With larger beds, channeling occurs in which the gas bypasses a majority of the particles [30]. Plugging and channeling make Type C particles non-ideal for mixing situations. Lastly, Type D contains large or very dense

particles ($d_s > 1000$ μm), which are prone to spouting. This causes an abrupt transition from the bubbling to the turbulent flow regime.

The catalyst particles used in the physical reactor have a density of 1750 kg/m^3 and the particle diameter has a bimodal distribution with peaks between 40−80 and 120−160 μm. Type A particles are preferable for the experimental reactor because they lack cohesion and facilitate bed expansion. For our numerical simulations, we use a diameter of 100 μm, which means that the particles can be classified as either Geldart Type A or Geldart Type B. We show in Chapter 4 that the simulations capture the particle behavior that occurs within the physical reactor with regard to v_{mf}.

1.4 Gas Introduction Methods

There are several commonly used bed configurations for introducing gas or other feedstocks into the bed besides a bottom plate distributor. One method is to introduce an upward-facing central jet of higher velocity in combination with the uniform velocity plate distributor maintained at v_{mf}. Feeding tubes are often used for inputting gases into the bed. Experimental [54, 7, 31, 68] and computational [46, 45, 58] studies of horizontal side feeding tubes are common in the literature. A central, downward-facing vertical feeding tube is utilized in our reactor to force gas and cellulose particles deep into the bed for catalytic fast pyrolysis. The use of central feeding tubes is less common in the literature, and thus the tubes' effects on the hydrodynamics of the bed is less predictable.

1.5 Deviations from Canonical Beds

Even if no gas is injected through the feeding tube, the presence of the tube will alter bubble formation and bed fluidization due to the obstruction caused by the tube. Additional complications of the flow can result from high flow rate through the tube.

1.5.1 Horizontal Tubes

Immersed horizontal tubes within fluidized beds have been shown empirically and numerically to alter fluidization and bubbling behavior [56, 35, 36, 5, 44]. Hull et al. [35] performed numerical simulations to determine the effects of horizontal tubes on the average bubble size and velocity. The authors compared their work to experimental studies [81] for verification. The tubes broke the rising bubbles into smaller bubbles, which then coalesced back into larger bubbles after rising above the tubes. The effect of the tubes is the retardation of growth and speed of the bubbles, resulting ultimately in smaller, slower bubbles.

Further studies by Hull et al. [36] considered the effect on mixing times with and without submerged horizontal tubes by tracking the mixing residence times of an added tracer gas jet. The location of the tracer gas inlet was a significant determining factor of mixing time, with a minimum mixing time occurring when the tracer gas was located in the center of the bed. For slower fluidizing velocities, tracer gas inlets located on the fringes of the bed led to mixing times on the order of two times longer than when the inlet was in the center of the bed. The authors concluded that local minima in mixing residence times occurred when both the tracer gas was injected centrally and when tubes were located either near the distributor plate or near the top of the solids.

The horizontal immersed tube studies confirm that bubble behavior, and therefore mixing times, are sensitive to not only the presence but also the location of obstructions relative to gas inlets. Mixing is quickest near the center of the bed, indicating that the walls have a strong influence in deterring mixing.

1.5.2 Vertical Tubes

Studies involving immersed vertical tubes and baffles have also shown that the presence of such obstructions within fluidized beds hinders bubble growth, which helps prevent slugging [63, 16, 57, 43, 66].

Ozawa et al. [57] employed a neutron radiography method on a fluidized bed to visualize and quantify void fractions for a bed with and without a vertical tube bank. The authors considered Geldart Type A and B particles with $d_s = 62$ μm and 218 μm, respectively. They found that the presence of the tubes reduced the bubble diameters for both cases, and that the tubes served as a dividing "guider" for the bubbles. Bubbles in a freely bubbling bed "wandered" throughout the bed in their trajectory; with the tubes, however, bubbles were "guided" vertically. Additionally, bubble diameter reduction was more prevalent in beds with a lower height-to-depth ratio and the change in bubble reduction was attenuated at higher ratios ($2 \leq H/D \leq 3$).

Our reactor includes one vertical tube through which gas is injected into the bed, and, because the reactor is enclosed and insulated, its effect on fluidization, bubble size, and mixing are unknown and require CFD simulations.

CHAPTER 2

THEORY AND MODEL

Although fluidized beds have been used in industry for decades, only recently, with advancements in computing power, has computational fluid dynamics (CFD) come to fuller fruition in predicting the behavior of fluidized beds. In the past, fluidized beds could only be modeled semi-empirically, theoretically, and with coarse-mesh CFD simulations. The behavior of such beds is dependent upon the fully closed Navier-Stokes equations. However, these exact equations cannot be solved without closure models to account for particle stress and strain, gas drag, and friction between particles. Developments and improvements in computing power in recent years have led to an extensive number of verified numerical studies of fluidized beds. These simulations and the methods employed are now accepted and commonplace for predicting bed behavior for a fluidized bed in standard configuration.

2.1 Governing Equations

The governing two-phase conservation equations used in ANSYS© Fluent are derived by Ishii [37] and applied to gas-solids flows by Enwald et al. [24]. We utilize the versions of these equations as reproduced by van Wachem et al. [75]. A summary of all the governing equations and closure models employed in this study is presented in the Appendix in Tables A.1, A.2, and A.3. All symbol and variable definitions can also be found in the List of Symbols. Further information about all models available in Fluent can be found in the Fluent Theory Guide [3].

The continuity equation for the gas phase g with velocity $\boldsymbol{v}_g$ is

$$\frac{\partial \alpha_g}{\partial t} + \nabla \cdot (\alpha_g \boldsymbol{v}_g) = 0; \tag{2.1}$$

for the solid phase s with velocity $\boldsymbol{v}_s$, the continuity equation is

$$\frac{\partial \alpha_s}{\partial t} + \nabla \cdot (\alpha_s \boldsymbol{v}_s) = 0. \tag{2.2}$$

Here, α_g represents the gas volume fraction and α_s represents the solids (catalyst) volume fraction. By conservation of mass, $\alpha_s + \alpha_g = 1$.

The two-phase gas/solids conservation of momentum equations are given by Enwald et al. [24], where

$$\rho_g \alpha_g \left(\frac{\partial \boldsymbol{v}_g}{\partial t} + \boldsymbol{v}_g \cdot \nabla \boldsymbol{v}_g \right) = -\alpha_g \nabla P + \nabla \cdot \alpha_g \bar{\bar{\tau}}_g + \alpha_g \rho_g \boldsymbol{g} - \beta(\boldsymbol{v}_g - \boldsymbol{v}_s) \tag{2.3}$$

is for the gas phase, and

$$\rho_s \alpha_s \left(\frac{\partial \boldsymbol{v}_s}{\partial t} + \boldsymbol{v}_s \cdot \nabla \boldsymbol{v}_s \right) = -\alpha_s \nabla P + \nabla \cdot \bar{\bar{\tau}}_s - \nabla P_s + \alpha_s \rho_s \boldsymbol{s} + \beta(\boldsymbol{v}_g - \boldsymbol{v}_s) \tag{2.4}$$

is for the solids phase. Here, $\bar{\bar{\tau}}_k$ is the viscous stress tensor for phase k, β is the interphase momentum transfer coefficient, P is the pressure shared by both phases, and P_s is the solids pressure due to particle-particle interactions described by kinetic theory.

The conservation of energy equation for phase k involves the specific enthalpy h_k and is given in the Fluent Theory Guide [3] as

$$\frac{\partial}{\partial t}(\alpha_k \rho_k h_k) + \nabla \cdot (\alpha_k \rho_k \boldsymbol{v}_k h_k) = \alpha_k \frac{\partial P_k}{\partial t} + \bar{\bar{\tau}}_k : \nabla \boldsymbol{v}_k - \nabla \cdot \boldsymbol{q}_k, \tag{2.5}$$

where $\boldsymbol{q}_k$ is the heat flux of phase k. For our simulations, there are no chemical reactions or heat source terms and thus $\boldsymbol{q}_k = 0$.

2.2 Closure Models

Closure of the momentum equations requires a description of the stresses on the particle. Chapman and Cowling [13] developed the kinetic theory of granular flow (KTGF) and this theory was furthered by Jenkins and Savage [39] and Lun et al. [52]. For our purposes, we list only the closure models relevant to our simulation of a densely packed bed. Additional information on other models can be found in the comparative studies of van Wachem et al. [75] and the Appendix.

2.2.1 Granular Temperature

Particle velocity variations are measured by the granular temperature Θ, where

$$\Theta = \frac{1}{3}\left\langle \boldsymbol{v}_s'^2 \right\rangle. \tag{2.6}$$

The granular temperature for the solid phase is analogous to the thermodynamic temperature for the gas phase.

The energy balance for granular energy is

$$\frac{3}{2}\left(\frac{\partial}{\partial t}(\alpha_s \rho_s \Theta) + \nabla \cdot (\alpha_s \rho_s \Theta \boldsymbol{v}_s)\right) = \left(-P_s \bar{\bar{I}} + \bar{\bar{\tau}}_s\right) : \nabla \boldsymbol{v}_s + \nabla \cdot (\kappa_s \nabla \Theta) - \gamma_s - J_s. \tag{2.7}$$

Here, κ_s is the solids thermal conductivity, γ_s is the dissipation of granular energy from inelastic particle collisions, and J_s is the dissipation of granular energy due to velocity fluctuations.

The dissipation term is given by Lun et al. [52] as

$$\gamma_s = 12(1-e^2)\frac{\alpha_s^2 \rho_s g_0 \Theta^{\frac{3}{2}}}{d_s\sqrt{\pi}}. \tag{2.8}$$

The coefficient of restitution e is usually close to 1 ($e = 0.9$ in our case); d_s and g_0 are the particle diameter and the radial distribution function, respectively.

Dissipation from velocity fluctuations is given as $J_s = \beta(\overline{\boldsymbol{v}_s' \cdot \boldsymbol{v}_g'} - \overline{\boldsymbol{v}_g' \cdot \boldsymbol{v}_s'})$. Closure of these terms is given by Louge et al. [50], where

$$J_s = \beta\left(3\Theta - \frac{\beta d_s(\boldsymbol{v}_g - \boldsymbol{v}_s)^2}{4\alpha_s\rho_s\sqrt{\pi\Theta}}\right). \tag{2.9}$$

Following the work of Syamlal et al. [71] and Boemer et al. [9], the energy balance for dense flows can be simplified by assuming that the granular energy is in steady state ($\frac{\partial}{\partial t}(\alpha_s \rho s \Theta) = 0$), the granular energy is dissipated locally ($J_s = 0$), and the convection $\nabla\cdot(\alpha_s\rho_s\Theta\boldsymbol{v}_s)$ and diffusion terms $\nabla\cdot(\kappa_s\nabla\Theta)$ can be neglected. The energy balance simplifies to

$$0 = \left(-P_s\bar{\bar{I}} + \bar{\bar{\tau}}_s\right) : \nabla\boldsymbol{v}_s - \gamma_s. \tag{2.10}$$

Here, the first term represents the generation of fluctuating energy due to solids shear. For dense flows, the remaining generation and dissipation terms dominate, so Equation (2.10) is a reasonable estimate [75]. Solving Equation (2.10) for the granular temperature gives,

$$\begin{aligned}\Theta = &\frac{-(K_1\alpha_s + \rho_s)\mathrm{tr}(\bar{\bar{D}}_s)}{2\alpha_s K_4} \\ &+ \frac{\sqrt{(K_1\alpha_s+\rho_s)^2\mathrm{tr}^2(\bar{\bar{D}}_s) + 4K_4\alpha_s[2K_3\mathrm{tr}(\bar{\bar{D}}_s^2) + K_2\mathrm{tr}^2(\bar{\bar{D}}_s)]}}{2\alpha_s K_4},\end{aligned} \tag{2.11}$$

with the abbreviations

$$
\begin{aligned}
K_1 &= 2(1+e)\rho_s g_0 \\
K_2 &= \frac{4}{3\sqrt{\pi}} d_s \rho_s (1+e)\alpha_s g_0 - \frac{2}{3} K_3 \\
K_3 &= \frac{d_s \rho_s}{2}\left(\frac{\sqrt{\pi}}{3(3-e)}\left[1+\frac{2}{5}(1+e)(3e-1)\alpha_s g_0\right] + \frac{8\alpha_s}{5\sqrt{\pi}} g_0 (1+e)\right) \\
K_4 &= \frac{12(1-e^2)\rho_s g_0}{d_s\sqrt{\pi}}.
\end{aligned}
\tag{2.12}
$$

When the flow is dilute, Equations (2.10) and (2.11) do not suffice and Equation (2.7) must be solved. The average solids volume fraction within our bed is between $60-100\%$ the maximum catalyst packing value. Since the bed is primarily dense rather than dilute, we employ the algebraic granular temperature formulation (Equation (2.11)).

2.2.2 Solids Pressure

The solids pressure P_s, given by Lun et al. [52], incorporates the granular temperature into the momentum equations with

$$P_s = \alpha_s \rho_s \Theta + 2 g_0 \alpha_s^2 \rho_s \Theta (1+e). \tag{2.13}$$

The two terms in the solids pressure represent the respective kinetic and collisional contributions due to particle-particle interactions.

2.2.3 Viscous Stress

The viscous stress tensor for phase k is

$$\bar{\bar{\tau}}_k = 2\mu_k \bar{\bar{D}}_k + \left(\lambda_k - \frac{2}{3}\mu_k\right) \mathrm{tr}(\bar{\bar{D}}_k)\bar{\bar{I}}, \tag{2.14}$$

where

$$\bar{\bar{D}}_k = \frac{1}{2}[\nabla \boldsymbol{v}_k + (\nabla \boldsymbol{v}_k)^\top]. \tag{2.15}$$

The solids bulk λ_s and shear μ_s viscosities must be modeled. Lun et al. [52] gives the solids phase bulk viscosity as

$$\lambda_s = \frac{4}{3}\alpha_s \rho_s d_s g_0 (1+e)\sqrt{\frac{\Theta}{\pi}}. \tag{2.16}$$

The solids shear viscosity is divided into two parts, the collisional contribution $\mu_{s,col}$ and the kinetic contribution $\mu_{s,kin}$, which together yield $\mu_s = \mu_{s,col} + \mu_{s,kin}$. According to Gidaspow [30], the collisional part is given as

$$\mu_{s,col} = \frac{4}{5}\alpha_s^2 \rho_s d_s g_0 (1+e)\sqrt{\frac{\Theta}{\pi}}, \tag{2.17}$$

and the kinetic part,

$$\mu_{s,kin} = \frac{1}{15}\sqrt{\pi\Theta}\rho_s d_s g_0 (1+e)\alpha_s^2 + \frac{1}{6}\sqrt{\pi\Theta}\rho_s d_s \alpha_s + \frac{10}{96}\sqrt{\pi\Theta}\frac{\rho_s d_s}{(1+e)g_0}. \tag{2.18}$$

2.2.4 Solids Thermal Conductivity

The solids thermal conductivity κ_s is considered when solving the full PDE for Θ. The Gidaspow model [30] is utilized when relevant:

$$\kappa_s = \frac{2}{(1+e)g_0}\left[1 + \frac{6}{5}(1+e)g_0\alpha_s\right]^2 \kappa_{dil} + 2\alpha_s^2 \rho_s d_s g_0 (1+e)\sqrt{\frac{\Theta}{\pi}}, \tag{2.19}$$

where the dilute phase granular conductivity is given by

$$\kappa_{dil} = \frac{75}{384}\rho_s d_s \sqrt{\pi\Theta}. \tag{2.20}$$

2.2.5 Frictional Stress

Frictional stresses occur at high solids volume fractions due to prolonged contact between particles. In Newtonian form, the frictional stress tensor $\bar{\bar{\sigma}}_f$ is written as

$$\bar{\bar{\sigma}}_f = P_f \bar{\bar{I}} + \mu_f \left[\nabla \boldsymbol{v} + (\nabla \boldsymbol{v})^\top \right]. \tag{2.21}$$

Frictional stresses are only considered when the solids volume fraction packs above the critical point $\alpha_{s,min}$. The stresses are added to the solids pressure and solids bulk viscosity, as described by kinetic theory in Equations (2.13), (2.17), and (2.18), such that

$$P_s = P_{kinetic} + P_f \tag{2.22}$$

and

$$\mu_s = \mu_{kinetic} + \mu_f. \tag{2.23}$$

The two most commonly used frictional stress models are those of Johnson and Jackson [40] and Schaeffer et al. [67] (furthered developed and implemented by Syamlal et al. [71]). We use the first of these models, in which the normal frictional stress P_f is modeled semi-empirically as

$$P_f = Fr \frac{(\alpha_s - \alpha_{s,min})^n}{(\alpha_{s,max} - \alpha_s)^p}, \tag{2.24}$$

where Fr, n, and p are empirically determined material constants and $\alpha_{s,max}$ is the maximum packing solids volume fraction (typically between $0.63-0.65$). Using the linear law proposed by Coulomb [17], the frictional shear viscosity is related to P_f by

$$\mu_f = P_f \sin \phi, \tag{2.25}$$

where ϕ is the particle's angle of internal friction. The empirical constants within this frictional stress model have not been determined for a wide range of particles. In addition,

although Johnson and Jackson [40] only give values for glass and polystyrene beads (d_s = 1800 μm and 1000 μm, respectively), the constants were not robustly determined, and as a result, van Wachem et al. [75] recommend that frictional stress models be used with caution.

We use the Johnson and Jackson [40] model, with typical values $Fr = 0.05$, $n = 2$, $p = 5$, $\phi = 25°$, and $\alpha_{s,min} = 0.6$ [75, 4]. Instabilities tend to occur when α_s increased well above $\alpha_{s,min}$ and so we set $\alpha_{s,min}$ closer to the packing limit of 0.63. Friction played the largest role when $v_{fl} < v_{mf}$, i.e., when the bed is very densely packed. For this reason, we use the frictional model to better match the experimental behavior of the bed below v_{mf}.

2.2.6 Radial Distribution Model

The radial distribution function g_0 increases the probability of particle collisions when α_s approaches the packing limit. The radial distribution function tends towards infinity at maximum packing and unity when the solids volume fraction approaches zero [75]. The Lun and Savage [51] radial distribution model is given as

$$g_0 = \left(1 - \frac{\alpha_s}{\alpha_{s,max}}\right)^{-2.5\alpha_{s,max}}. \tag{2.26}$$

2.2.7 Drag Model

The Gidaspow drag model [30] for the interphase momentum transfer coefficient β is used for densely packed beds. It combines the Ergun equation [25] and the Wen and Yu drag model [79], such that

$$\beta = \begin{cases} 150\frac{\alpha_s^2\mu_g}{\alpha_g d_s^2} + \frac{7}{4}\frac{\rho_g\alpha_s|\boldsymbol{v}_g - \boldsymbol{v}_s|}{d_s} & \text{for } \alpha_s \geq 0.2 \\ \frac{3}{4}C_d\frac{\rho_g\alpha_s\alpha_g|\boldsymbol{v}_g - \boldsymbol{v}_s|}{d_s}\alpha_g^{-2.65} & \text{for } \alpha_s < 0.2. \end{cases} \tag{2.27}$$

Rowe [65] relates the drag coefficient C_D to the relative Reynolds number Re with

$$C_D = \begin{cases} \frac{24}{\mathrm{Re}}\left[1 + 0.15(\mathrm{Re})^{0.687}\right] & \text{for Re} < 1000 \\ 0.44 & \text{for Re} \geq 1000, \end{cases} \tag{2.28}$$

where

$$\mathrm{Re} = \frac{\alpha_g \rho_g |\boldsymbol{v}_g - \boldsymbol{v}_s| d_s}{\mu_g}. \tag{2.29}$$

2.3 Semi-empirical correlations

Before the prevalence of CFD models, correlations based on theory and empirical studies were used to predict fluidization in fluidized beds. These include correlations for the minimum fluidization velocity, the minimum bubbling velocity, and bed expansion. The empirical correlations discussed below provide a basis of comparison for CFD simulations, especially where experimental data is not available. It should be noted that all of the empirical correlations are derived for a standard cylindrical fluidized bed configuration with a uniform fluidizing gas flow, without the central feeding tube employed in our reactor. For this reason, we first run simulations to validate our numerical model with a standard-geometry, tubeless fluidized bed.

2.3.1 Minimum fluidization velocity

The minimum fluidization velocity equation originates from Stokes [70] for viscous resistance of a spherical particle of diameter d_s in a fluid with viscosity μ_g and velocity v. The viscous drag is

$$F_v = 3\pi\mu_g v d_s. \tag{2.30}$$

Setting the force equal to the effective gravitational force, $\frac{\pi d_s^3}{6}(\rho_s - \rho_g)g$, we solve for the terminal falling velocity of a single spherical particle,

$$v_0 = \frac{d_s^2(\rho_s - \rho_g)g}{18\mu_g}. \tag{2.31}$$

Following the same logic for a single particle's terminal velocity, Robinson [64] suggested that a collection of uniform particles in a fluidized bed could be suspended with a minimum fluidization velocity of

$$v_{mf} = K\frac{d^2(\rho_s - \rho_g)}{\mu_g}g, \tag{2.32}$$

where K is an empirically determined constant. Typically, subsequent correlations for v_{mf} follow the form of Equation (2.32).

Davies and Richardson [21] averaged experimental data for various catalysts ($55 \leq d_s \leq 142$ μm and $945 \leq \rho_s \leq 1230$ kg/m^3) to obtain a value for K. The Davies and Richardson [21] correlation for minimum fluidization velocity is

$$v_{mf} = 0.0078\frac{d^2(\rho_s - \rho_g)}{\mu_g}g. \tag{2.33}$$

Another correlation that is often used for fine Geldart Type A particles was derived by Baeyens [6]. For 48 gas/solid systems with $20 \leq d_s \leq 70$ μm and $1117 \leq \rho_s \leq 3920$ kg/m^3, Abrahamsen and Geldart [1] confirmed the correlation as the best-fit equation for v_{mf},

$$v_{mf} = \frac{0.0009(\rho_s - \rho_g)^{0.934}d^{1.8}g^{0.934}}{\mu_g^{0.87}\rho_g^{0.066}}. \tag{2.34}$$

Many other authors [55, 65, 79, 27, 62, 12] have similar correlations, based on different experimental data. A discussion and summary of various v_{mf} correlations can be found in [80] in which Wu et al. study the effect of temperature on the minimum fluidization velocity. The gas viscosity and density are both functions of temperature, and thus v_{mf} can vary dramatically depending on the operating temperature.

Our research operates with particles most similar to those of Davies and Richardson [21], Baeyens [6], and Abrahamsen and Geldart [1] – catalysts with $d_s = 100$ μm and $\rho_s = 1750$ kg/m^3. To fully understand the fluidization process, we compare these correlation models, our experimental data, and the computational data generated.

2.3.2 Minimum Bubbling Velocity

The minimum bubbling velocity is defined as the velocity at which bubbles begin to form within a fluidized bed [29]. The traditional equation for v_{mb} applied only for air at ambient conditions and was given by Geldart as

$$v_{mb} = 100 d_s. \tag{2.35}$$

Abrahamsen and Geldart [1] updated this equation to account for gases with different densities and viscosities. Based on their data, they found the correlation

$$v_{mb} = 2.07 \exp\left(0.716 F_{45}\right) \frac{d_s \rho_g^{0.06}}{\mu^{0.347}}, \tag{2.36}$$

where F_{45} is the fraction of particles less than 45 μm.

2.3.3 Bed expansion

Bed expansion with respect to v_{mf} and v_{mb} is empirically derived by Abrahamsen and Geldart [1] as

$$\frac{H_{mb}}{H_{mf}} = \left(\frac{v_{mb}}{v_{mf}}\right)^{0.22}. \tag{2.37}$$

The minimum fluidization velocity, the minimum bubbling velocity, and the bed expansion correlations provide comparison points for our simulations of a standard configuration fluidized bed.

CHAPTER 3

SIMULATION

3.1 Modeling methods

The computational fluid dynamics (CFD) of a fluidized bed are typically simulated using either the Lagrangian or the Eulerian method. The Lagrangian method applies Newtonian physics to each particle, tracking its position, velocity, momentum, and how particles collide and interact with each other and the walls. The Eulerian method, on the other hand, is a control-volume approach, which treats each phase as interpenetrating continua [30].

3.1.1 Lagrangian Method

Examples of Lagrangian simulations include Hoomans et al.'s simulations of 40,000 particles treated as hard spheres [32], Bokkers et al.'s numerical and experimental study with 30,000 particles [10], Chu and Yu's particle-fluid flows with 3000−20,000 particles [14], and more recently, Wang et al. simulations with 42,000 particles [78]. For further information on Lagrangian method simulations, see reviews written by Deen et al. [22] and Zhu et al. [82].

The discrete particle method (DPM) is the state-of-the-art, Lagrangian particle-tracking method to discretely account for all but interparticle cohesive forces each particle encounters. The method is widely accepted as an accurate way to simulate fluidized beds [22, 83, 82], but it is severely limited due to the computational expenses involved in tracking a large number of particles.

Most discrete tracking simulations only consider beds with up to 50,000 particles. Our lab-scale reactor uses 90 grams of ZSM5 catalyst particles, which is on the order of 10^7

particles, a prohibitively expensive number of particles to track. A more practical approach is to instead use the faster Eulerian method.

3.1.2 Eulerian Method

The Eulerian method discretizes the problem into a mesh consisting of cells within which conservation equations (mass, momentum, and energy) are applied. The method requires less computing power and is therefore more frequently applied for solving dense, multiphase flows. Because both the gas and solids phase are treated as liquids, this method is often referred to as an Euler-Euler (or Euler-Granular, due to the granular modeling of the solids phase) approach, as opposed to an Euler-Lagrange approach in which a control volume is used for the gas but not the particles.

In theory, the finer the mesh, the more accurately the Eulerian approach can describe multiphase flow. Often, mesh refinement studies are included within the literature [53, 48, 33] to ensure that for a given mesh size, a finer mesh still tends towards the same solution. Inaccurate bed expansion values for unrefined grids is a primary problem for the simulation of fine particles. In the following section we discuss studies on the limitations of the Eulerian approach when applied to fine particles.

3.2 Simulation of Geldart Type A Particles

Good agreement with experimental data has been found for Geldart Type B and D particles for numerical simulations using the Eulerian approach [60, 34, 72]. However, numerical simulations of Type A particles continue to challenge scientists and engineers. In the past, simulations tended toward unrealistic solutions with overestimation of bed expansion on the order of two times the experimental bed height [26, 2, 53, 84]. Based on the work of Parmentier et al. [59] and Di Renzo and De Maio [23], Wang et al. [76] noted that the cause of this overestimation may be due to insufficient resolution of subgrid structures. These structures,

such as small bubbles, could be resolved by decreasing the mesh size such that cell lengths δ are $2-4$ times the particle diameter [76].

Another theory on expansion overprediction is that structures begin to cluster due to interparticle forces (IPFs) [28, 53, 84, 74]. Mckeen and Pugsley [53] conducted numerical studies with fluid catalytic cracking (FCC) particles ($d_s = 75$ μm) and found that by scaling down the drag coefficient by a factor of about $0.2-0.3$, their simulations were able to match experimental data. They argued that the particle clusters at a subgrid level necessitate this scaling factor. The agglomerate cluster size they find to be $\sim 135-170$ μm, about two times the actual particle size.

Following the work of Mckeen and Pugsley [53], other authors validated Geldart Type A simulations with experimental data through the use of drag scaling factors [19, 33, 48, 47]. Lindborg et al. [48] created a varying scaling factor specifically designed to match the pressure vs. fluidizing velocity measured experimentally in their laboratory. Similarly, Hosseini et al. [33] found an ideal drag scaling factor of 0.1 in order to find agreement with experimental bed expansion, but they note that the scaling factor varies with fluidizing velocity and a general scaling factor model has not been fully established for Type A particles.

It has been shown that for Type A particles of size $d_s = 50-105$ μm, IPFs are negligible since the fluidization characteristics can be fully described with frictional stresses [49, 69, 73]. To validate this, Wang et al. [78] performed simulations using the DPM to explore IPFs at different particle diameters ($50 \leq d_s \leq 150$ μm and $\rho_s = 1500$ kg/m^3). They found that for Type A particles larger than 55 μm, IPFs are essentially negligible, and a refined mesh resolves the subgrid bubbling structures needed to properly predict bed expansion. The authors stressed, however, that their studies only involved cold flow under atmospheric pressure, and that the role of inter-particle cohesive forces could also be a function of temperature.

Wang et. al [77] also performed an Eulerian-Eulerian CFD study to determine the effect of mesh size on determining v_{mb} and compared their results to the semi-empirical v_{mb} model derived by Abrahamsen & Geldart [1] (Equation (2.36)). The authors found that with a course mesh ($\delta = 10 \times d_s$), v_{mb} was overpredicted by over 77% times the literature value due to lack of resolving any bubbles. When the mesh size was changed to $\delta = 2.7 \times d_s$, v_{mb} was determined to be within 20% times the empirically determined v_{mb}. Wang et. al considered there to be no bubble phase in a simulation if within every cell in the catalyst bed, $\alpha_s > 0.2$. Conversely, the authors declared a simulation to have a bubble if within any cell in the bed $\alpha_s < 0.15$. We use a similar criteria for defining the bubble phase and finding v_{mb}.

In recent years, the advancement of computing capability makes meshes of minute size realizable. Here, we use a mesh resolution of ~ 30 cells/cm. This equates to about 3.4 times the particle diameter for $d_s = 100$ μm, which fits well within the $2-4$ range for sufficient resolution.

3.3 Physical Parameters

In our simulations, we approximate the ZSM5 catalysts to have a mean particle diameter of $d_s = 100$ μm, a density of $\rho_s = 1750$ kg/m^3, and the total catalyst bed to have a mass of $m = 90$ g. Since the actual distribution of particle sizes in the reactor is bimodal, we can expect some discrepancy between the simulations and the experimental reactor.

The fluidizing gas properties, in particular ρ_g and μ_g, vary according to the operating temperature. Due to the high temperature necessary for CFP, the experimental reactor is operated at $T = 773$ K. Table 3.1 shows the effect of temperature on the density (based on the ideal gas law) and dynamic viscosity of helium and the argon and nitrogen tracer gases [61, 42, 11].

The minimum fluidization velocity is also a function of temperature as well (see Equations (2.32), (2.33), and (2.34)). Since the difference in densities ($\rho_s - \rho_g$) is dominated by the

T (K)	ρ_{He} (kg/m^3)	ρ_{Ar} (kg/m^3)	ρ_{N_2} (kg/m^3)	μ_{He} (10^{-5} kg/(m·s))	μ_{Ar}(10^{-5} kg/(m·s))	μ_{N_2} (10^{-5} kg/(m·s))
300	0.163	1.623	1.138	1.991	2.261	1.788
400	0.122	1.217	0.854	2.436	2.883	2.210
500	0.098	0.974	0.683	2.847	3.426	2.579
600	0.081	0.811	0.569	3.235	3.914	2.911
773	0.063	0.630	0.442	3.863	4.676	3.418
800	0.061	0.609	0.427	3.956	4.779	3.494

Table 3.1: Helium, argon, and nitrogen density and dynamic viscosity vs. temperature.

solids density, which is not a function of temperature, the primary parameter in evaluating the dependence of v_{mf} on temperature is the gas viscosity. Between room temperature (300 K) and the operating conditions (773 K), the viscosity of helium gas increases by a factor of 1.94. Thus we can expect the minimum fluidization velocity to be inversely proportional to this ratio, i.e., 0.51 times less. Experimentally, the gas is initially at room temperature when it begins to proceed down the tube. However, the gas is rapidly heated by the inside wall of the feeding tube. We assume that by the time the gas proceeds down the tube, it has reached the full 773 K, and as such isothermal conditions are met.

3.4 Geometry

The geometry of our simulated model is based on the experimental reactor, which is 60.96 cm (24 in) tall and has a 5.08 cm (2 in) outer diameter, a 4.925 cm (1.939 in) internal diameter, and a 1.27 cm (0.5 in) diameter feeding tube down the center axis of the reactor extending to a depth of 1.524 cm (0.6 in) above the distributor plate. Due to computational expenses, we simulate a height of $H = 12.7$ cm (5 in) with a radius of $R = 2.54$ cm (1 in) on a 2D axisymmetric mesh. Because the flow becomes constant above the catalyst bed and the catalyst bed height is only about 4−6 cm, the height restriction is a reasonable assumption. A mesh resolution of 29.528 cells/cm ($\sim$ 30 cells/cm = 75 cells/R) is used, which introduces

some slight rounding on the tube locations. The feed tube is 19 cells wide with a radius of $R_T \approx 0.643$ cm and extends 46 cells above the bottom fluidizer inlet: $H_T \approx 1.558$ cm. The meshes with and without the feeding tube can be seen in Figure 3.1. In the figure, the mesh is mirrored over the axis of symmetry. The meshes are also described in Table 3.2.

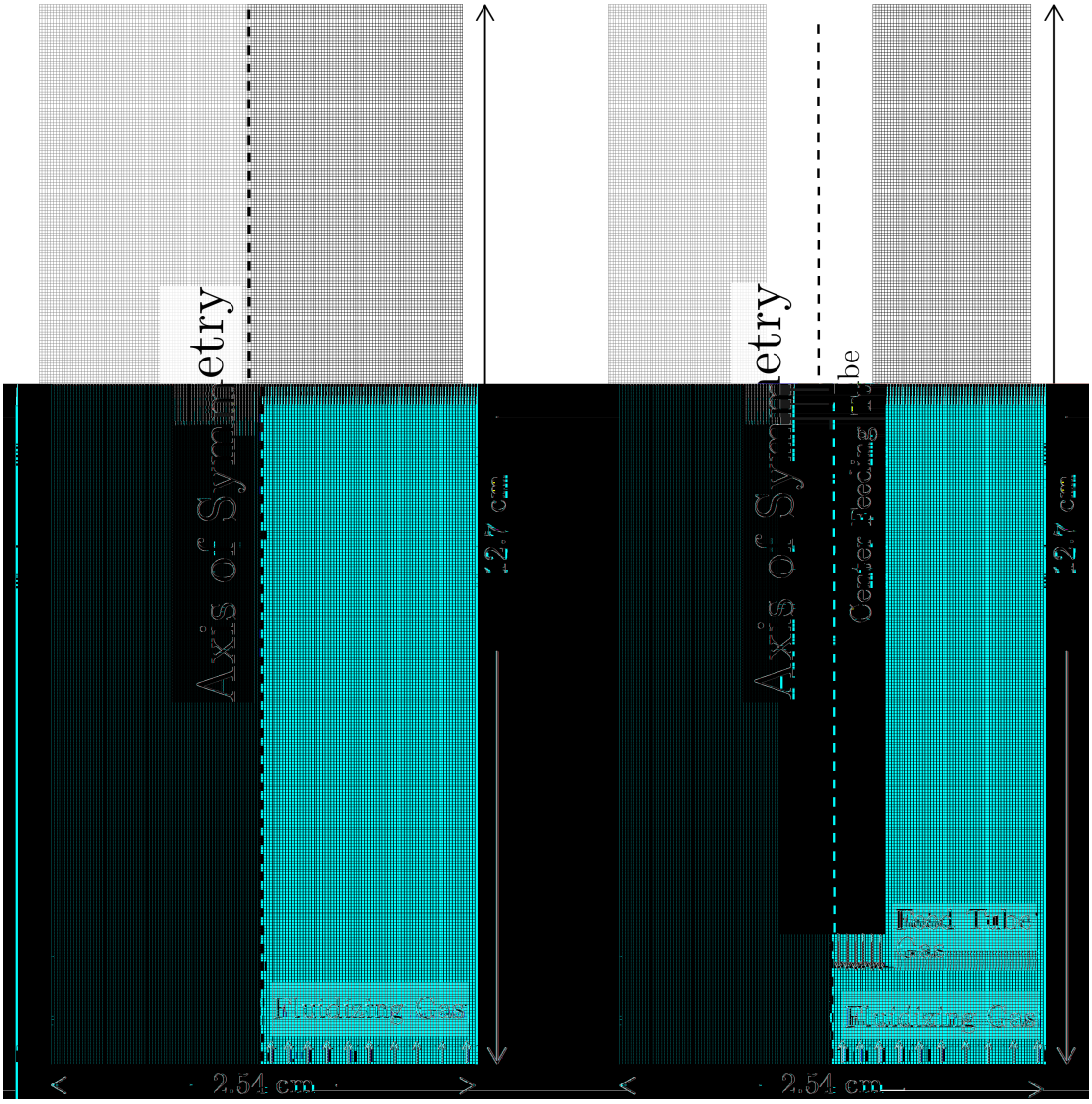

Figure 3.1: CFD meshes at ~ 30 cells/cm mesh resolution for meshes without a tube (left) and with a tube (right). Gas inlets, the feeding tube, and the axis of symmetry are indicated.

Cells/Radius	Grid Size (μm)	δ/d_s	Total Cells	Tube
75	338.67	3.39	28125	No
75	338.67	3.39	21938	Yes

Table 3.2: Summary of 2D axisymmetric meshes of the reactor with and without the tube.

3.5 Boundary Conditions

The commercial software ANSYS© Fluent 14.0 is utilized for the simulations. The following subsections detail the boundary conditions for each wall, inlet, and outlet used for these simulations. Information regarding the boundary conditions and options available in Fluent is available in the Fluent User's Guide [4].

3.5.1 Walls

We consider one (two) wall(s) for the mesh without (with) a feed tube. Each wall is set to the boundary type `wall`. For both walls, a free-slip boundary condition is prescribed for the two phases due to the uncertainty of boundary layers in such a two-phase flow. The free-slip condition is applied by setting the `Specified Shear` for both the x- and y-components to a constant 0 Pa. The walls are set to be stationary with temperature = 773 K, wall thickness = 0 m, and heat generation = 0 W/m^3. One can define the material of the walls by creating a steel material from the Fluent database of materials. However, since heat-transfer is insignificant in an isothermal reactor, the material of the walls does not matter in these simulations. Lastly, for the two tracer gases, the wall boundary condition is set to `Zero Diffusive Flux`.

3.5.2 Axis

The internal axis of symmetry is defined by selecting the type `axis`. No further specification is needed beyond selecting both 2D in the Fluent start-up menu and `Axisymmetric`

in the general options. When a 2D axisymmetric setting is used, derivatives with respect to ϕ are set equal to 0, where in a cylindrical coordinate system (r, z, ϕ), ϕ is the angular coordinate, r is the radial coordinate, and z is the axial coordinate.

3.5.3 Inlets

Each of the inlets is set to type `velocity-inlet` for both phases. This ensures Dirichlet boundary conditions [15], a constant inlet velocity (non-zero value for gas, zero value for solids), which we prescribe in the axial direction. The inlet solids volume fraction is set to 0 as well, and the inlet granular temperature is set to 0.001 m^2/s^2 to account for minor velocity fluctuations. For the mixture of the two phases, the `Supersonic/Initial Gauge Pressure` is set to 0 Pa.

For simulations without a feed tube, there is only one inlet to consider. The fluidizer inlet gas velocities are set to one of the following, depending on the simulation: v_{fl} = 0.1, 0.2, 0.3, 0.4, 0.6, 0.8, 0.9, 1.0, 1.5, 2.0, or 3.0 cm/s.

Two sets of simulations are performed with the feeding tube based on flow rate configurations used with the experimental reactor, the results of which are in development for a paper [41]. In the first set, five simulations were run to study the effect of gas distribution between the feed tube and the bottom fluidizer. This was achieved by changing the percentage of the flow from the feed tube Q_{ft} ($Q_{ft}/Q_{total} \approx$ 8%, 17%, 33%, 51%, or 68%) while keeping the total gas flow rate constant ($Q_{total} \approx$ 55 cm^3/s), where $Q_{total} = Q_{ft} + Q_{fl}$. For this set of simulations, $Q_{total} \approx 8 \times Q_{mf}$, where Q_{mf} is the fluidizer flow rate at the experimentally determined minimum fluidization velocity (Q_{mf} = 6.917 cm^3/s, v_{mf} = 0.363 cm/s). Experimentally, the best aromatic yield was found when Q_{ft}/Q_{total} = 34%. The second set of simulations are used to study the effect of changing the total flow rate ($Q_{total}/Q_{mf} \approx$ 3, 4, 6, or 8) while holding constant the ratio $Q_{ft}/Q_{total} \approx$ 34%.

v_{fl} $\left(\frac{\text{cm}}{\text{s}}\right)$	Q_{ft} $\left(\frac{\text{cm}^3}{\text{s}}\right)$	Q_{fl} $\left(\frac{\text{cm}^3}{\text{s}}\right)$	Q_{total} $\left(\frac{\text{cm}^3}{\text{s}}\right)$	$\frac{Q_{total}}{Q_{mf}}$	v_{ft} $\left(\frac{\text{cm}}{\text{s}}\right)$	$\frac{Q_{ft}}{Q_{total}}$ (%)
0.1	-	1.91	1.91	0.28	-	-
0.2	-	3.81	3.81	0.55	-	-
0.3	-	5.72	5.72	0.83	-	-
0.4	-	7.62	7.62	1.10	-	-
0.6	-	11.43	11.43	1.65	-	-
0.8	-	15.24	15.24	2.20	-	-
0.9	-	17.15	17.15	2.48	-	-
1	-	19.05	19.05	2.75	-	-
1.5	-	28.58	28.58	4.13	-	-
2	-	38.10	38.10	5.51	-	-
3	-	57.15	57.15	8.26	-	-

$\frac{Q_{ft}}{Q_{total}}$ (%)	Q_{ft} $\left(\frac{\text{cm}^3}{\text{s}}\right)$	Q_{fl} $\left(\frac{\text{cm}^3}{\text{s}}\right)$	Q_{total} $\left(\frac{\text{cm}^3}{\text{s}}\right)$	$\frac{Q_{total}}{Q_{mf}}$	v_{ft} $\left(\frac{\text{cm}}{\text{s}}\right)$	v_{fl} $\left(\frac{\text{cm}}{\text{s}}\right)$
7.74	4.33	51.63	55.96	8.09	3.33	2.55
17.48	9.75	46.01	55.76	8.06	7.49	2.27
33.21	18.41	37.04	55.45	8.02	14.16	1.83
51.11	28.16	26.94	55.10	7.97	21.65	1.33
68.24	37.37	17.40	54.77	7.92	28.73	0.86

$\frac{Q_{total}}{Q_{mf}}$	Q_{ft} $\left(\frac{\text{cm}^3}{\text{s}}\right)$	Q_{fl} $\left(\frac{\text{cm}^3}{\text{s}}\right)$	Q_{total} $\left(\frac{\text{cm}^3}{\text{s}}\right)$	$\frac{Q_{ft}}{Q_{total}}$ (%)	v_{ft} $\left(\frac{\text{cm}}{\text{s}}\right)$	v_{fl} $\left(\frac{\text{cm}}{\text{s}}\right)$
3.15	7.24	14.57	21.82	33.21	5.57	0.72
4.21	9.66	19.43	29.09	33.21	7.43	0.96
6.31	14.49	29.14	43.63	33.21	11.14	1.44
8.41	19.32	38.86	58.18	33.21	14.85	1.92

Table 3.3: Flow rate configurations for 3 sets of CFD simulations: a set without a tube in which the fluidizer velocity is varied, a set of runs with the tube and a near-constant Q_{total} as a function of Q_{ft}, and a set of tube simulations with a constant Q_{ft}/Q_{total} as a function of Q_{total}.

The experimental gas velocities were used for the simulations, but as these were calculated using the experimental internal diameter (4.925 cm) rather than the 5.08 cm diameter used in simulation, upon back-calculation of the flow rates, we find that the flow rate ratios deviate slightly from the experimental runs. This introduces a relatively small error, which bears no difference in the interpretation of the results. As noted in the summary of flow conditions in Table 3.3, Q_{total} differs at most by 2.17% in the first set of runs.

3.5.4 Outlet

The outlet is set to `pressure-inlet`, in which a constant pressure (0 Pa above atmospheric) is prescribed and the gas and solids velocities compensate appropriately (known as a Neumann boundary condition [15]). Due to the constant flow rates at the top of the reactor, we rarely observed backflow occurring in the simulations. The backflow conditions are as follows: $\alpha_s = 0$, $T = 773$ K, $Y_{Ar} = 0$, $Y_{N_2} = 0$, and $\Theta = 0.0001$ m^2/s^2, where Y_{Ar} and Y_{N_2} are the respective argon and nitrogen mass fractions.

3.5.5 Internal field

The initial uniform solids volume fraction in the interior of the bed is determined by the height of the bed and the initial mass of zeolite catalysts. For a bed mass m, the following equation must be satisfied within a standard (i.e. no tube) fluidized bed configuration:

$$\alpha_s = \frac{m}{\pi R^2 h \rho_s}, \tag{3.1}$$

where h is the catalyst bed height. A maximum-packed bed occurs when $\alpha_s = \alpha_{s,max} = 0.63$ and corresponds to $h = 4.242$ cm in our case. Above this bed height, $\alpha_s = 0$ and thus, $\alpha_g = 1$. A loosely packed bed ($\alpha_s = 0.44$) is commonly used as an initial condition corresponding to $h = 5.8$ cm within a tubeless bed. When the tube is considered, the bed height for a given mass will be higher due to the volume occupied by the tube.

The initial solution for the tube simulations comes from a simulation by Saba Almalkie, a previous researcher for the EFRI group. Due to differences in these simulations, slight changes had to be made such as the tube size (from $R_T = 0.457$ cm to 0.643 cm), the slip condition on the walls (from no-slip to free-slip), the frictional model (from none to the model described in Section 2.2.5), the particle diameter (from $d_s = 50$ μm to 100 μm), the mesh size (from ~ 39 cells/cm to ~ 30 cells/cm), and the operating temperature (from 900 to 773 K). These changes were primarily made by mapping the solution from the older mesh to the newer. The internal temperature was adjusted by patching a new temperature into each cell, and subsequently, the properties of the gas were changed according to Table 3.1. Lastly, because we mapped the previous solution onto a mesh with a larger feed tube, we had to add the appropriate amount of mass back to the system to conserve the 90 grams of catalyst. This mass was added well above the bed and was allowed to fall into the bed. After the new catalyst mixed with the rest of the bed, gas velocities were changed according to the tube configurations in Table 3.3. This method of solution mapping was utilized due to difficulties in initializing the solution caused by instabilities from the frictional stress model.

The internal initial conditions for the cases without the tube were set to an operating temperature of 773 K. All these cases were run using the $v_{fl} = 1.0$ cm/s simulation as the initial solution.

3.6 Numerical Method

ANSYS© Fluent gives a wide range of selection for solution methods, numerical schemes, and solvers. These were selected based on simulation consistency, accuracy, and stability. The multiphase model in Fluent uses the Semi-Implicit Method for Pressure-Linked Equations (SIMPLE) method. Further information for this solving method can be found in the Fluent Theory and User's Guides [3, 4] and in the CFD book by Chung [15]. We typically set the number of SIMPLE iterations to $60-100$ iterations per time-step, with time-steps

	p	ρ	Body Forces	Momentum	α_s	Θ	Energy	Tracer Gases
Tubeless runs	0.2	0.5	0.6	0.4	0.2	0.2	0.5	-
Tube runs	0.2	0.4	0.8	0.4	0.2	0.1	0.6	0.8

Table 3.4: Under-relaxation factors.

varying between 10^{-5} and 10^{-4} s. We used modified, smaller under-relaxation factors for better stability. These are listed in Table 3.4.

To initialize the flow field for tubeless cases, the numerical solvers were first order implicit in time and first order upwind for solving the momentum equation. After about 100 time-steps, we switched to a second order implicit solver in time and a higher order QUICK scheme. The QUICK scheme is especially designed for quadrilateral meshes and uses a solution-dependent weighted average between the second-order upwind scheme and central interpolation [3]. QUICK was also used for tube simulations and for solving all variables (momentum, volume fraction, granular temperature, energy, and tracer gases). Additionally, a least-squares, cell-based method was used for solving gradients. Generally, the time-step was increased to 10^{-4} s after a quasi-steady state was reached unless simulation stability required us to reduce the time-step.

The simulations were run on $4-32$ processors each, and took, on average, 200 h to simulate 10 s of simulation time. We noted that the benefits of parallel processing tapered off after about 8 processors due to the relatively low number of total cells ($\sim 28,000$ cells).

3.7 Quantifying Mixing

Once a fluidized bed has reached a quasi-steady state, we study its long-term behavior and quantify the fluctuating quantities by using time-averaged statistics such as the mean and variance. A quasi-steady state is reached after about $2-4$ s of simulation time. This

is determined by performing statistical analyses on different simulation durations until the results are statistically stable. These are discussed furthermore in Chapter 4.

3.7.1 Tracer Gases

Using Fluent, tracer gases are introduced at each inlet to track mixing. The gas phase is primarily helium (He) but at the fluidizer inlet, a nitrogen (N_2) gas is introduced at 2% mole fraction and at the feed tube inlet, an argon (Ar) gas is introduced, also at 2% mole fraction. The mole fraction X_i of species i can be converted to a mass fraction Y_i via the following relationship:

$$Y_i = X_i \times \frac{M}{M_i}, \tag{3.2}$$

where M and M_i are the average molecular weights of the mixture and the species i, respectively. It follows that within each cell, $Y_{He} + Y_{Ar} + Y_{N_2} = 1$.

The free-stream mass fraction is pertinent to the inlet from which the tracer gas is introduced and represents the maximum possible mass fraction of that tracer gas. We calculate the free-stream mass fractions of Ar and N_2, defined as Y_{Ar}^{∞} and $Y_{N_2}^{\infty}$, respectively,

$$\begin{aligned} Y_{Ar}^{\infty} &= X_{Ar} \times \frac{M}{M_{Ar}} = 0.02 \times \frac{(4.0026 + 39.948)\ \text{kg/kgmol}}{39.948\ \text{kg/kgmol}} = 0.169217 \\ Y_{N_2}^{\infty} &= X_{N_2} \times \frac{M}{M_{N_2}} = 0.02 \times \frac{(4.0026 + 28.0134)\ \text{kg/kgmol}}{28.0134\ \text{kg/kgmol}} = 0.124981. \end{aligned} \tag{3.3}$$

In addition, the free-stream mass fractions of each tracer gas are the same for every case, regardless of the velocity at the inlets.

The well-mixed case occurs when the tracer gases and the fluidizing helium gas mix proportional to the volume or mass flow rate of each component. The outlet mass fractions of each tracer gas represents such a well-mixed case, and we denote these as the ideal mass

fractions Y_{Ar}^{ideal}, $Y_{N_2}^{ideal}$, and Y_{He}^{ideal}. We use Y_{N_2} to demonstrate how $Y_{N_2}^{ideal}$ can be found. An alternate form of the mass fraction can be defined in terms of mass flow rates:

$$\begin{aligned} Y_{N_2}^{ideal} = Y_{N_2}^{outlet} &= \frac{\dot{m}_{N_2}^{outlet}}{\dot{m}_{mix}^{outlet}} \\ &= \frac{\dot{m}_{N_2}^{fl}}{\dot{m}_{mix}^{ft} + \dot{m}_{mix}^{fl}}, \end{aligned} \tag{3.4}$$

where, ft and fl are the respective feed tube and bottom fluidizer inlets. In order to calculate the mass flow rate, we first find the density of the mixture at each inlet:

$$\rho_{mix}^{fl} = \left(\frac{Y_{N_2}^{\infty}}{\rho_{N_2}} + \frac{Y_{He}^{fl}}{\rho_{He}} \right)^{-1} = \left(\frac{Y_{N_2}^{\infty}}{\rho_{N_2}} + \frac{1 - Y_{N_2}^{\infty}}{\rho_{He}} \right)^{-1} \tag{3.5}$$

$$\rho_{mix}^{ft} = \left(\frac{Y_{Ar}^{\infty}}{\rho_{Ar}} + \frac{Y_{He}^{ft}}{\rho_{He}} \right)^{-1} = \left(\frac{Y_{Ar}^{\infty}}{\rho_{Ar}} + \frac{1 - Y_{Ar}^{\infty}}{\rho_{He}} \right)^{-1}, \tag{3.6}$$

and then multiply each these by the respective volume flow rate to get the mass flow rates:

$$\dot{m}_{mix}^{fl} = Q_{fl} \times \rho_{mix}^{fl} \tag{3.7}$$

$$\dot{m}_{mix}^{ft} = Q_{ft} \times \rho_{mix}^{ft} \tag{3.8}$$

$$\dot{m}_{N_2}^{fl} = Y_{N_2}^{\infty} \times \dot{m}_{mix}^{fl}. \tag{3.9}$$

These mass flow rates depend upon the volume flow rates at the inlets (see Table 3.3) and the gas densities (see Table 3.1). We tabulate these ideal mass fractions in the following subsection (see Table 3.5) and discuss their significance in determining the mixture fraction and the ideal mixture fraction.

3.7.2 Mixture Fraction

The mixture fraction ξ is our main measure for quantifying the mixing of the feed tube tracer gas with the remainder of the bed. The mixture fraction is a conserved scalar typically used in combustion problems in turbulent mixing cases [8, 3]. Here, there are no chemical reactions occurring, simply diffusive mixing between the two tracer gases (Ar and N_2) and the dominant He fluidizing gas. We define the mixture fraction such that $\xi = 1$ when the maximum possible concentration of the Ar feed tube tracer gas component is attained and $\xi = 0$ when the component concentration is 0:

$$\xi = \frac{Y_{N_2}^{\infty} - Y_{N_2}}{Y_{N_2}^{\infty}}, \tag{3.10}$$

Thus, at the feeding tube inlet, where the argon concentration is at its maximum and the nitrogen concentration is negligible, $\xi = 1$; at the fluidizer inlet, where $Y_{Ar} = 0$, $\xi = 0$.

Note that in the well-mixed case, the mixture fraction will not be equal to 1. Combining Equation (3.10) with Equations (3.4), (3.9), (3.8), and (3.7) yields the following equation for the ideal mixture fraction, denoted with ξ_{ideal}:

$$\begin{aligned}
\xi_{ideal} &= \frac{Y_{N_2}^{\infty} - \frac{Y_{N_2}^{\infty} \times \dot{m}_{mix}^{ft}}{Q_{ft} \times \rho_{mix}^{ft} + Q_{fl} \times \rho_{mix}^{fl}}}{Y_{N_2}^{\infty}} \\
&= 1 - \frac{Q_{ft} \times \rho_{mix}^{ft}}{Q_{ft} \times \rho_{mix}^{ft} + Q_{fl} \times \rho_{mix}^{fl}} \\
&= \frac{Q_{fl} \times \rho_{mix}^{fl}}{Q_{ft} \times \rho_{mix}^{ft} + Q_{fl} \times \rho_{mix}^{fl}} \\
&= \left(\frac{Q_{ft} \times \rho_{mix}^{ft}}{Q_{fl} \times \rho_{mix}^{fl}} + 1 \right)^{-1}.
\end{aligned} \tag{3.11}$$

ξ_{ideal} and Y_{N_2} are tabulated in Table 3.5 for each simulation with a feed tube.

$\frac{Q_{ft}}{Q_{total}}$ (%)	$Y_{N_2}^{ideal}$	ξ_{ideal}
7.74	0.115	0.081
17.48	0.102	0.182
33.21	0.082	0.344
51.11	0.059	0.524
68.24	0.038	0.693

$\frac{Q_{total}}{Q_{mf}}$	$Y_{N_2}^{ideal}$	ξ_{ideal}
3.15	0.082	0.344
4.21	0.082	0.344
6.31	0.082	0.344
8.41	0.082	0.344

Table 3.5: Ideal N_2 tracer gas mass fraction and mixture fraction for each simulation with the feeding tube.

3.7.3 Volume-weighted Statistics

The following subsections describe the method of calculating the volume-weighted mean and variance for an arbitrary, cell-centered quantity $O(r, z, t)$. Spatial averages are denoted with an overbar $\overline{O}$ while time averages are denoted as $\left\langle O \right\rangle$. Since we are simulating a 3D fluidized bed using a 2D axisymmetric slice, simulation outputs are dependent only on r, z, and t, the radial distance from the axis of symmetry to the cell center, the axial distance from the fluidizer to the cell center, and the simulation time, respectively. Statistics on the solids volume fraction and the mixture fraction will be performed as a function of bed height, bed radius, and over the catalyst bed as a whole.

In order to inspect the mixing quality within the bed, we employ primarily 4 statistical quantities applied over the entire space of the catalyst bed and over a statistically steady time period (4 s). These quantities are scaled to show relevant information. The first is $\varepsilon = \left\langle \overline{\alpha_s} \right\rangle / \alpha_{s,max}$, the time-ensemble, volume-weighted mean within the catalyst bed of the solids volume fraction, normalized by the maximum packing limit. Secondly, we analyze

$\psi = \left\langle \overline{\alpha_s'^2} \right\rangle / \alpha_{s,max}'^2$, the normalized variance of the catalyst. The maximum possible variance $\alpha_{s,max}'^2$ is determined by considering the variance between two samples, one at the lowest possible value ($\alpha_s = 0$) and the other at the highest possible value ($\alpha_s = 0.63$). It follows that $\alpha_{s,max}'^2 = (0.63 - 0)^2/2 = 0.19845$. The parameter ψ shows how much the catalyst changes inside the bed, and is a good measure of the amount of bubbling within the bed. A slugging bed, for instance, will exhibit a high value of ψ as large voidages rise over the width of the bed followed by the catalyst, filling the space in the wake.

Although ε and ψ are useful in probing the mixing of the catalyst, we are essentially interested in how well the feed tube tracer gas (representing the gasified cellulose) mixes throughout the bed. The time-ensemble, volume-weighted mean of the mixture fraction scaled by the ideal mixture fraction $\theta = \left\langle \overline{\xi(r)} \right\rangle / \xi_{ideal}$ provides a good measure of how well this tracer gas is mixed. A well-mixed bed should thus have $\theta \approx 1$.

The most important statistic we use in quantifying the mixing potential of the feed tube gas is $\Phi = \left\langle \overline{\xi'^2} \right\rangle / \left\langle \overline{\xi} \right\rangle^2$, the time-ensemble, volume-weighted variance of the mixture fraction, which we scale by the mean mixture fraction squared. We use this scaling in order to acquire a dimensionless quantity that signifies not just a low variance, well-mixed case but also one with a significant amount of tracer gas present. The mixing parameter Φ is equivalent to the squared coefficient of variation, where the coefficient of variation is the standard deviation over the mean. In our case, the lower Φ is, the better we consider the case for the mixing of the feed tube gas. It is this value that we compare to the aromatic yield since stoichiometrically, better mixed cellulose gas and catalyst produces more aromatics.

This set of quantities $\{\varepsilon, \psi, \theta, \Phi\}$ is also calculated vs. bed height ($\varepsilon(z)$, $\psi(z)$, $\theta(z)$, and $\Phi(z)$) and vs. bed radius ($\varepsilon(r)$, $\psi(r)$, $\theta(r)$, and $\Phi(r)$). For instance, $\Phi(r) = \left\langle \overline{\xi(r)'^2} \right\rangle / \left\langle \overline{\xi(r)} \right\rangle^2$, $\Phi(z) = \left\langle \overline{\xi(z)'^2} \right\rangle / \left\langle \overline{\xi(z)} \right\rangle^2$, and so forth. Two other statistical quantities that are relevant especially to the cases run without the tube are the bed expansion $\Omega = \frac{h - h_{mf}}{h_{mf}}$ and the volume of the bed occupied by the bubble phase $\chi = \frac{V_{\alpha_s \leq 0.15}}{V_{bed}}$ (see the bubble phase definition from

Section 3.2). Thus the set of quantities we analyze for simulations without a tube is {ε, ψ, Ω, χ}

3.7.4 Statistical Convergence

Before calculating any time-averaged statistics, we must first gauge a statistically steady time period (T_S) over which to perform our analyses. We look specifically at the convergence of the four mixing parameters ε, ψ, θ, and Φ with respect to a range of sampling time lengths (T_S = 0.1, 0.2, 0.5, 1.0, 1.5, 2.0, 2.5, 3.0, 3.5, 4.0, 4.5, 5.0 s) from the latest time for each simulation. If, for a specific case the mixing parameters all have converged to a statistically significant value, then we use the converged sample time for all statistical analyses. Because some cases mix better than others, the sampling time can be shorter for some cases ($T_S \sim 2$ s) than for others ($T_S \sim 4$ s).

3.7.5 Volume-weighted Mean

We weigh each cell by its respective volume before averaging, since the 2D axisymmetric assumption means the outer cells within the cylinder occupy a greater volume than the inner cells. Horizontal slice averages convert the three-dimensional (two dimensions in space, one dimension in time) value $O(r, z, t)$ into a one-dimensional vector as a function of z, $\left\langle \overline{O(z)} \right\rangle$. For each z location, we integrate over the radius and time, dividing by the volume of the slice and the time over which the average is taken, t_i to t_f:

$$\left\langle \overline{O(z)} \right\rangle = \frac{1}{t_f - t_i} \frac{2\pi\Delta z}{V(z)} \int_{t_i}^{t_f} \int_{0}^{R} O(r, z, t)\ r\ dr\ dt, \tag{3.12}$$

where the volume of the horizontal slice $V(z)$ is dependent on whether or not $z \geq H_T$:

$$V(z) = \pi(R^2 - R_T^2(z))\Delta z, \tag{3.13}$$

and

$$R_T(z) = \begin{cases} 0 & \text{for } z < H_T \text{ (below feeding tube)} \\ R_T & \text{for } z \geq H_T \text{ (above feeding tube).} \end{cases} \tag{3.14}$$

Since we utilize discrete time-steps, the integral can be written as multiple summations. The discrete time-ensemble, volume-weighted radial mean of a quantity O is therefore

$$\left\langle \overline{O(z)} \right\rangle = \frac{1}{N} \frac{2\Delta r}{R^2 - R_T^2(z)} \sum_{i=1}^{N} \sum_{r=R_T(z)}^{R} O(r, z, t)\ r. \tag{3.15}$$

Vertical slice averages do not require a strict volume-weighting since cells in the axial direction have the same volume. We follow the formulation above to derive an equation for the time-ensemble, volume-weighted axial mean. The averages must be taken from the bottom of the bed to the height of the catalyst at each radial point, and so we must have some knowledge of what the bed height h is at each radial point r and at each time t, denoted with $h(r, t)$. This bed height, is found by scanning from the top of the reactor down until $\alpha_s(r, z, t) > 0.2$, at which point $h(r, t) = z$.

The time-ensemble, volume-weighted axial mean of $O(r, z, t)$ is, then,

$$\left\langle \overline{O(r)} \right\rangle = \frac{2\pi r \Delta r}{t_f - t_i} \int_{t_i}^{t_f} \int_{0}^{h(r,t)} \frac{O(r, z, t)}{V(r, t)}\ dz\ dt, \tag{3.16}$$

where

$$V(r, t) = 2\pi r \Delta r h(r, t). \tag{3.17}$$

For discrete data with N samples in time, Equation (3.16) simplifies to

$$\left\langle \overline{O(r)} \right\rangle = \frac{1}{N} \sum_{i=1}^{N} \sum_{z=0}^{h(r,t)} \frac{O(r, z, t)}{h(r, t)}. \tag{3.18}$$

3.7.6 Volume-weighted Variance

The volume-weighted variance can be derived in similar fashion to the volume-weighted mean, except using the square of the difference between the current value $O(r,z,t)$ and the respective time-ensemble mean, $\left\langle\overline{O(z)}\right\rangle$ or $\left\langle\overline{O(r)}\right\rangle$. The time-ensemble, volume-weighted radial variance of $O(r,z,t)$ is denoted as $\left\langle O'^2(z)\right\rangle$ and is given by

$$\left\langle\overline{O'^2(z)}\right\rangle = \frac{1}{t_f - t_i}\frac{2\pi\Delta z}{V(z)}\int_{t_i}^{t_f}\int_{0}^{R}\left[O(r,z,t) - \left\langle\overline{O(z)}\right\rangle\right]^2 r\ dr\ dt, \tag{3.19}$$

which simplifies in discrete form to

$$\left\langle\overline{O'^2(z)}\right\rangle = \frac{1}{N}\frac{2\Delta r}{R^2 - R_T^2(z)}\sum_{i=1}^{N}\sum_{r=R_T(z)}^{R}\left[O(r,z,t) - \left\langle\overline{O(z)}\right\rangle\right]^2 r. \tag{3.20}$$

For vertical slices, the time-ensemble, volume-weighted axial variance of $O(r,z,t)$, denoted as $\left\langle O'^2(r)\right\rangle$, is

$$\left\langle\overline{O'^2(r)}\right\rangle = \frac{2\pi r\Delta r}{t_f - t_i}\int_{t_i}^{t_f}\int_{0}^{h(r,t)}\frac{\left[O(r,z,t) - \left\langle\overline{O(r)}\right\rangle\right]^2}{V(r,t)}\ dz\ dt, \tag{3.21}$$

which simplifies to

$$\left\langle\overline{O'^2(r)}\right\rangle = \frac{1}{N}\sum_{i=1}^{N}\sum_{z=0}^{h(r,t)}\frac{\left[O(r,z,t) - \left\langle\overline{O(r)}\right\rangle\right]^2}{h(r,t)}. \tag{3.22}$$

3.7.7 Bed Mean and Variance

In order to quantitatively compare cases with different inlet velocities, we average statistics over the entirety of the bed. To calculate the bed average, we perform a time-ensemble,

volume-weighted average over all space within the bed and over all time such that

$$\left\langle \overline{O} \right\rangle = \frac{2\pi}{t_f - t_i} \int_{t_i}^{t_f} \int_{0}^{R_T} \int_{0}^{h(r,t)} \frac{O(r,z,t)\ r}{V_{bed}(t)}\ dz\ dr\ dt \tag{3.23}$$

where the volume of the bed at each time t is

$$V_{bed}(t) = 2\pi \int_{0}^{R_T} \int_{0}^{h(r,t)} r\ dz\ dr, \tag{3.24}$$

or, as a summation,

$$V_{bed}(t) = 2\pi \Delta z \Delta r \sum_{r=0}^{R_T} \sum_{z=0}^{h(r,t)} r. \tag{3.25}$$

Equation (3.23) is converted discretely to give the time-ensemble, volume-weighted bed mean of $O(r,z,t)$:

$$\left\langle \overline{O} \right\rangle = \frac{1}{N} \sum_{i=1}^{N} \frac{\sum_{r=0}^{R_T} \sum_{z=0}^{h(r,t)} O(r,z,t)\ r}{\sum_{r=0}^{R_T} \sum_{z=0}^{h(r,t)} r} \tag{3.26}$$

The time-ensemble, volume-weighted bed variance of $O(r,z,t)$, is similarly given as

$$\left\langle \overline{O'^2} \right\rangle = \frac{2\pi}{t_f - t_i} \int_{t_i}^{t_f} \int_{0}^{R_T} \int_{0}^{h(r,t)} \frac{\left[O(r,z,t) - \left\langle \overline{O} \right\rangle\right]^2\ r}{V_{bed}(t)}\ dz\ dr\ dt, \tag{3.27}$$

whose discrete form is

$$\left\langle \overline{O'^2} \right\rangle = \frac{1}{N} \sum_{i=1}^{N} \frac{\sum_{r=0}^{R_T} \sum_{z=0}^{h(r,t)} \left[O(r,z,t) - \left\langle \overline{O} \right\rangle\right]^2 r}{\sum_{r=0}^{R_T} \sum_{z=0}^{h(r,t)} r}. \tag{3.28}$$

The time-ensemble, volume-weighted variance within the catalyst bed, henceforward referred to as simply the bed variance, is the main metric used for determining mixing within the fluidized bed. The next chapter includes the simulation results and data analyses following the time-ensemble, volume-weighted statistical methods described above.

CHAPTER 4

RESULTS AND DISCUSSION

In this chapter, we first present no-feeding-tube simulation results to determine the minimum fluidization velocity, fluidization behavior, and the minimum bubbling velocity. Next, we show the results of simulations run with the tube (see Section 3.5.3 for setup details). The goal of these simulations is to relate the set of statistical quantities $\{\varepsilon, \psi, \theta, \Phi\}$ with the experimental product yields. The simulations provide visualization of the internal reactor flows, which helps illustrate the effect of different flow rate configurations on product yields. Finally, based on what we observe from the simulations, we offer suggested flow rate configurations for optimal mixing in a fluidized bed reactor.

4.1 Standard Configuration Fluidized Bed Simulations

Ten simulations were run in a standard, i.e. tubeless fluidized bed configuration with a mesh resolution of $\sim$ 30 cells/cm at fluidizing velocities between $0.1-3.0$ cm/s. These simulations were run to calculate the minimum fluidization velocity, the minimum bubbling velocity, and to analyze the internal flow behavior without the feed tube. The results are compared to both experiment and literature models for $\{\varepsilon, \psi, \Omega, \chi\}$, the set of parameters discussed in Section 2.3.

4.1.1 Determination of the Minimum Fluidization Velocity

Experimentally, the minimum fluidization velocity was determined by inserting a pressure probe at the top and another at the bottom of the catalyst bed and recording the average

pressure drop across the bed given a constant fluidizing velocity without any gas flowing from the feeding tube [41]. The fluidizing gas velocity was both increased and decreased to find the time-averaged pressure drop at that velocity. Different pressure drop curves were observed for the increasing and the decreasing velocity cases due to hysteresis of the fluidization process (see Figure 4.1). The minimum fluidization velocity v_{mf} was taken to be the fluidizing velocity at which the slope of the pressure curve changed significantly. The pressure drop found is measured between single points in space at the bottom and top of the bed, and averaged in time.

The simulations run in ANSYS© Fluent were initialized with a fluid velocity well above v_{mf} ($v_{fl} = 1.0$ cm/s) and then adjusted to the higher or lower velocities. After the pressure at the inlet readjusted to changes in velocity, we time-averaged the inlet pressure across the entire inlet. Additionally, we calculated the standard deviation in time to investigate the fluctuations in pressure about the mean. Figure 4.1 shows the experimental results for increasing and decreasing the fluidizing velocity, the inlet pressure from Fluent, and v_{mf} as determined by the Abrahamsen & Geldart [1] and the Davies & Richardson [21] literature models.

From Figure 4.1, we note that when increasing the fluidizing velocity in laboratory experiments, the pressure drop behavior is marked by a sharp peak followed by a short trough, which is indicative of hysteresis in the process of fluidization since the particles are initially packed closely and held together by friction and gravity. Thus, the decreasing velocity experimental runs are generally used as the more accurate measurement. We observe a significant change in the slope of the pressure vs. velocity in the decreasing-velocity case between $v_{fl} = 0.3{-}0.4$ cm/s, consistent with the experimentally determined minimum fluidization velocity $v_{mf} \approx 0.363$ cm/s [41]. The value of the minimum fluidization velocity for the CFD results is also in good agreement with the literature value of $v_{mf} \approx 0.3{-}0.4$ cm/s. In addition, we note that the average inlet pressure decreases while the standard deviation

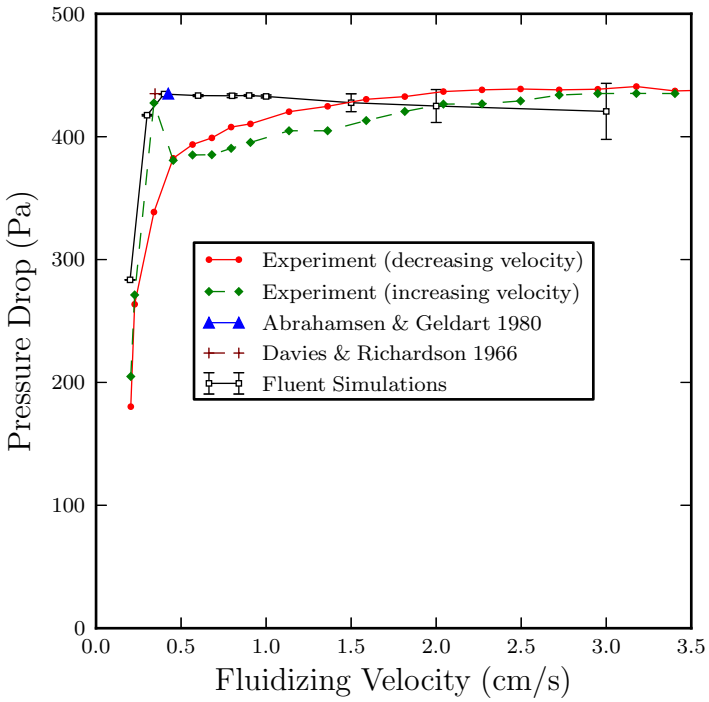

Figure 4.1: Minimum fluidization velocity determination via pressure drop vs. fluidizing velocity for Fluent simulations (bars indicate 2 standard deviations above and below the mean), the experimental reactor, and literature models.

increases dramatically with higher velocity ($v_{fl} > 1.0$ cm/s). There is thus a marked difference between simulations run below and above $v_{fl} = 1.0$ cm/s. The standard deviation bars demonstrate that the inlet pressure always fluctuates close to the experimentally determined pressure ($\sim$ 435 Pa), and the averaged inlet pressure at $v_{fl} = 3.0$ cm/s is only 3.3% lower than the experimental pressure at this velocity.

The Fluent simulations include a frictional model that accounts for frictional forces between particles at close packing ($\alpha_{s,min} = 0.6$). The maximum packing value of the catalyst volume fraction is set to $\alpha_{s,max} = 0.63$. Without the use of this friction model, the pressure drop curves were constant around 435 Pa for all Fluent simulations, including those below

the minimum fluidization velocity. This illustrates that the frictional model played a large role in producing pressure curves that agree with the experimental pressure curves.

4.1.2 Determination of the Minimum Bubbling Velocity

To visualize fluidization and analyze the qualitative differences between flows with $v_{fl} >$ 1.0 cm/s and $v_{fl} <$ 1.0 cm/s, we look at contour plots of the catalyst volume fraction for different velocities (see Figure 4.2). First, we note that at $v_{fl} <$ 0.4 cm/s, there are no changes in bed height or the packing of the catalyst, since $v_{fl} < v_{mf}$. With v_{fl} between 0.4 and 0.8 cm/s, fairly uniform bed expansion occurs with no bubbling. When $v_{fl} \geq$ 0.9 cm/s,

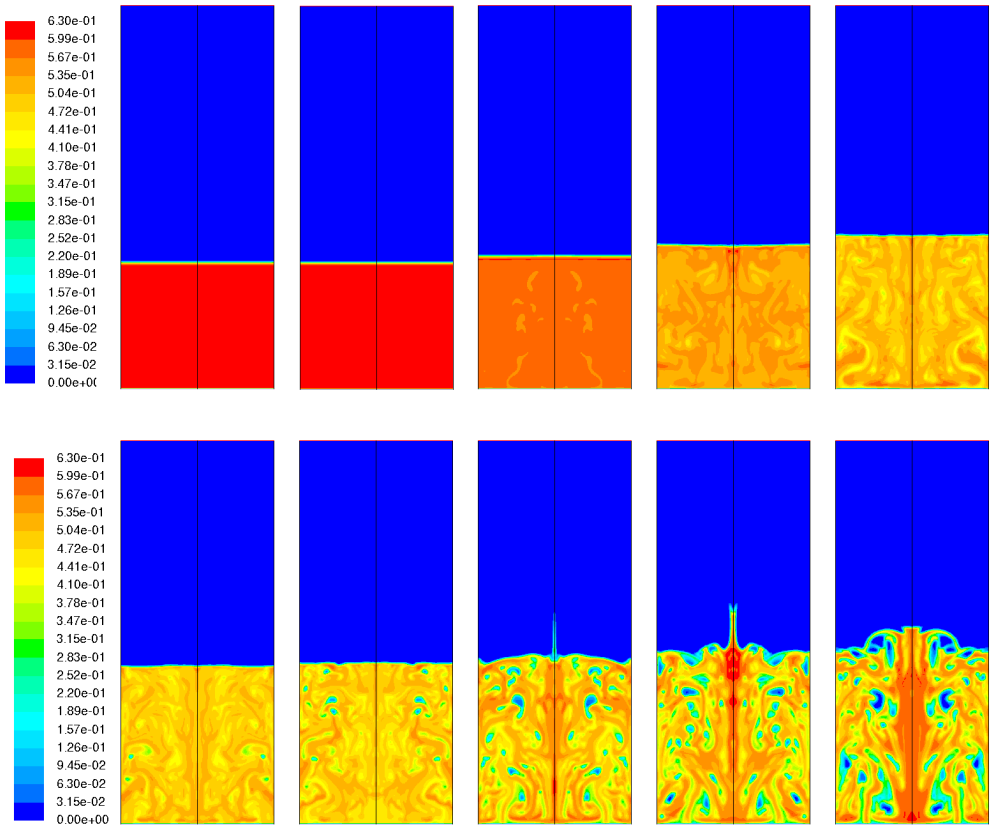

Figure 4.2: Catalyst volume fraction profiles for (top, from left to right) $v_{fl} =$ 0.2, 0.3, 0.4, 0.6, and 0.8 cm/s and (bottom, from left to right) $v_{fl} =$ 0.9, 1.0, 1.5, 2.0, and 3.0 cm/s.

bubbles begin to rise throughout the bed. It is commonly known that for Geldart Type A particles, such as this catalyst, $v_{mb}/v_{mf} > 1$ [29]. This indicates that we should expect bed expansion before bubbling, as the simulations do indeed show.

In order to determine v_{mb} from the simulations, we look at the parameter χ, the percentage of the bed occupied by the bubble phase. Additional parameters we would like to consider are the scaled average catalyst volume fraction ε within the bed, the bed expansion Ω, and the scaled bed variance of the catalyst ψ. These are plotted in Figure 4.3.

The bed expansion Ω and ε follow very similar trends when one is viewed on an inverted scale from the other. This is expected, since, in general, $h \propto \alpha_s^{-1}$ (see Equation 3.1). There is no significant bed expansion until $v_{fl} > 0.3$ cm/s, followed by a roughly linear increase in Ω until $v_{fl} = 1.0$ cm/s, and then a less steep slope of Ω vs. v_{fl} for $v_{fl} > 1.0$ cm/s. These

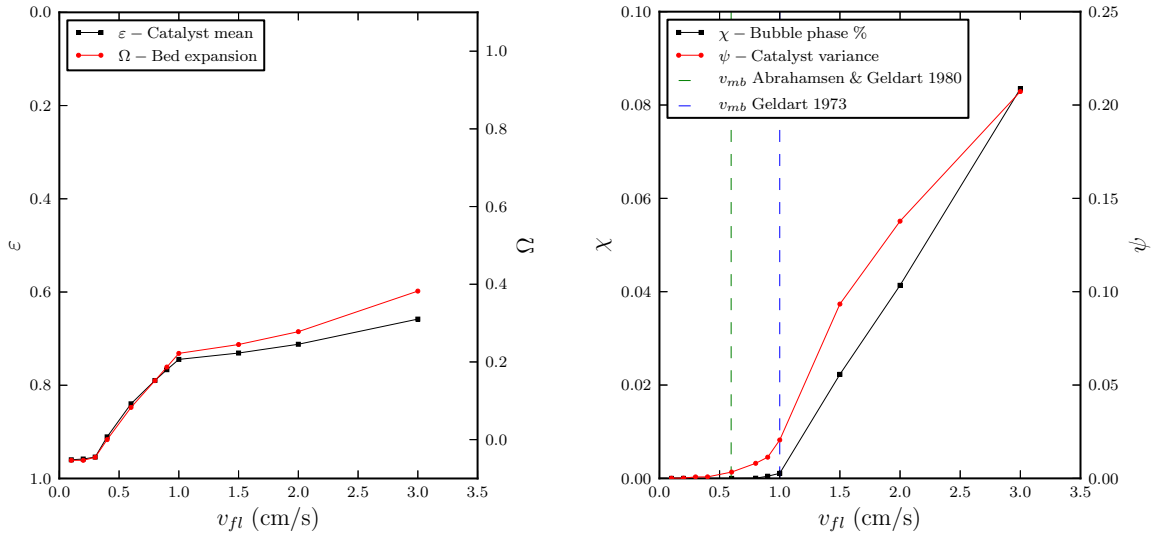

Figure 4.3: Four measures of the transition to the bubbling regime: (left) ε and Ω, (right) χ and ψ for tubeless Fluent simulations, where $\varepsilon = \frac{\langle \overline{\alpha_s} \rangle}{\alpha_{s,max}}, \Omega = \frac{h - h_{mf}}{h_{mf}}$, $\chi = \frac{V_{\alpha_s \leq 0.15}}{V_{bed}}$, and $\psi = \frac{\langle \overline{\alpha_s'^2} \rangle}{\alpha_{s,max}'^2}$.

observations agree with those noted from the catalyst contours in Figure 4.2 and, in addition, serve to quantify the bed expansion vs. fluidization velocity.

The dimensionless catalyst variance parameter ψ and the fraction of the bed occupied by the bubble phase χ exhibit very similar trends. In particular, both parameters dramatically increase with velocity for $v_{fl} > 1.0$ cm/s. We find that $v_{fl} = 0.9$ cm/s is the lowest velocity at which bubbling occurs, indicating that $v_{mb} \approx 0.9$ cm/s. The Abrahamsen & Geldart [1] model, which accounts for changes in gas properties, predicts v_{mb} significantly lower ($v_{mb} \approx 0.6$ cm/s) than either the CFD determined v_{mb} or the simpler literature model described by Geldart [29]. The simulation and the simpler literature model, however, are in very close agreement with $v_{mb} \approx 1.0$ cm/s.

Although small bubbles do form at $v_{fl} = 0.9$ and 1.0 cm/s, it is not until $v_{fl} = 1.5$ cm/s that a significant amount of the bed (2%) is occupied by the bubble phase in addition to a significant increase in catalyst variance. The change in internal bed bubbling at and above this fluidizing velocity provides a strong explanation for the observed changes in expansion rates and in the variance of the catalyst. The catalyst variance parameter serves to reinforce the fact that more bubbling means a higher variance in the catalyst.

Lastly, we compare the literature model for h_{mb}/h_{mf}, given by Equation (2.37), with the CFD results. For this exercise, we declare $v_{mb} = 0.9$ cm/s and $v_{mf} = 0.4$ cm/s. This gives the following relationship:

$$\begin{aligned} \frac{h_{mb}}{h_{mf}} &= \frac{5.207 \text{ cm}}{4.382 \text{ cm}} = 1.187 \\ &\approx \left(\frac{v_{mb}}{v_{mf}}\right)^{0.22} = \left(\frac{0.9 \text{ cm/s}}{0.4 \text{ cm/s}}\right)^{0.22} = 1.195. \end{aligned} \tag{4.1}$$

We find very good agreement with the empirical correlation of Abrahamsen & Geldart. Our simulations yield a h_{mb}/h_{mf} ratio that is only 0.7% lower than the empirical model predicts.

This relationship held true even though the value we found for v_{mb} was about 50% higher than the corresponding literature model predicted.

4.2 Effect of Gas Distribution

To test the effect of the gas distribution between the feed tube and fluidizer inlets, five simulations were run with varying ratios of the feed tube gas flow to the total gas flow rate ($Q_{ft}/Q_{total} \approx 8\%$, 17%, 33%, 51%, and 68%) and a constant total flow rate ($Q_{total} \approx 55$ cm^3/s) (see Tables 3.3 and 4.1).

4.2.1 Visualization

The catalyst volume fraction α_s, the Ar feeding tube tracer gas mass fraction Y_{Ar}, and the axial velocity of the catalyst v_s after the tracer gas is well-mixed are shown in Figure 4.4. From Figure 4.4a, we note that the $Q_{ft}/Q_{total} \approx 8\%$, 17%, and 33% cases (hereafter f8, f17, and f33, respectively) all have similar α_s profiles, bed heights, and bubble sizes. The $Q_{ft}/Q_{total} \approx 51\%$ and 68% cases (hereafter f51 and f68, respectively), however, show a marked difference with a lower bed height, a denser bed, and spouts of particles along the feeding tube wall. The feeding tube tracer gas profiles appear to show higher variance in these latter two cases (see Figure 4.4b), particularly with a high Ar concentration along

Case abbr.	$\frac{Q_{ft}}{Q_{total}}$ (%)	Q_{total} $\left(\frac{\text{cm}^3}{\text{s}}\right)$	$\frac{Q_{total}}{Q_{mf}}$	v_{ft} $\left(\frac{\text{cm}}{\text{s}}\right)$	v_{fl} $\left(\frac{\text{cm}}{\text{s}}\right)$
f8	7.74	55.96	8.09	3.33	2.55
f17	17.48	55.76	8.06	7.49	2.27
f33	33.21	55.45	8.02	14.16	1.83
f51	51.11	55.10	7.97	21.65	1.33
f68	68.24	54.77	7.92	28.73	0.86

Table 4.1: Flow rate configurations and abbreviations for simulations with a near-constant Q_{total} as a function of Q_{ft}.

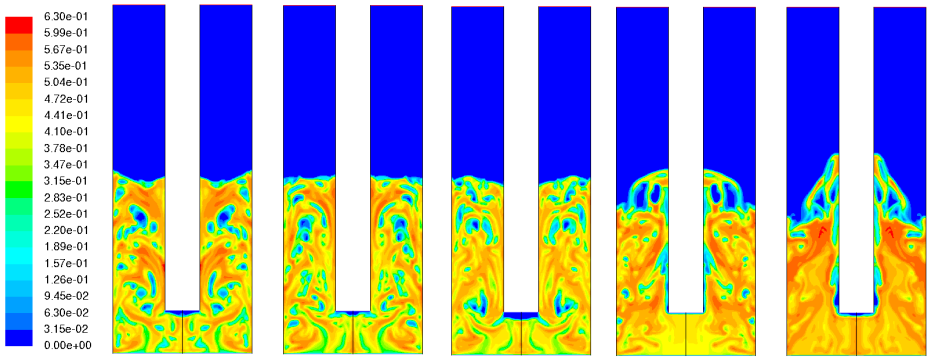

(a) α_s

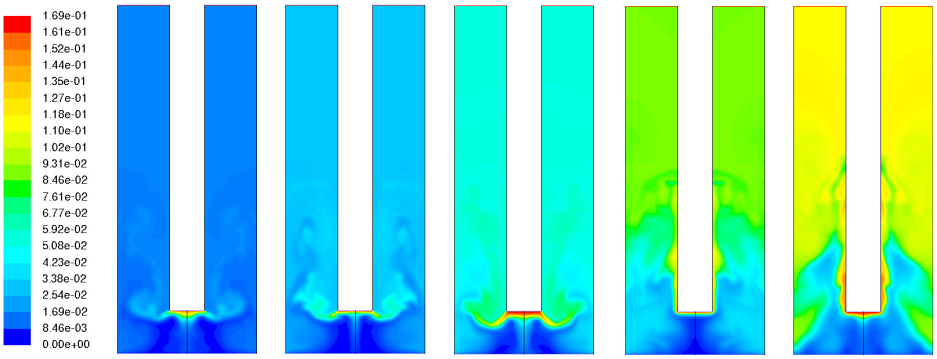

(b) Y_{Ar}

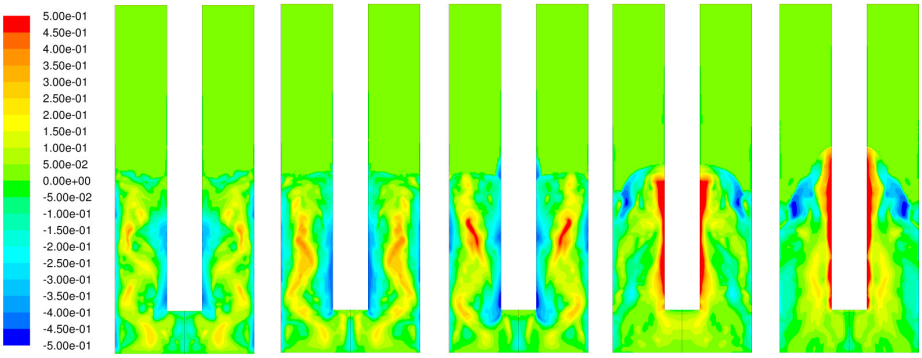

(c) v_s

Figure 4.4: Time snapshots of contour plots of (a) the catalyst volume fraction α_s, (b) the feed tube tracer gas mass fraction Y_{Ar}, and (c) the catalyst axial velocity magnitude v_s for Fluent simulations with a feed tube with a constant total flow rate $Q_{total} \approx 55$ cm^3/s and different ratios of Q_{ft}/Q_{total} (left to right: 8%, 17%, 33%, 51%, and 68%).

the feed tube. In Figure 4.4c, we note different flow behavior with the catalyst having a downward flow along the feeding tube wall for f8, f17, and f33, and with the catalyst having a high upward velocity along the feeding tube wall for f51 and f68.

4.2.2 Statistical Convergence

As discussed in Section 3.7.4, we must find T_S for each case, the time period over which the four mixing parameters $\{\varepsilon, \psi, \theta, \Phi\}$ are in a statistically steady state. The four parameters are plotted vs. sample length in Figure 4.5. The ε vs. T_S plot shows that for all five cases, full convergence occurs after about 1.5 s. The normalized variance of the catalyst volume fraction converges after 3 s. The mean mixture fraction over the ideal mixture fraction θ converges after about 2 s for f8, f17, f33, and f51 and after about 4 s for f68. Lastly, Φ shows a similar set of convergence times with all five cases in full convergence for a sampling time period of ~ 4 s. For consistency, we use the same time period of $T_S = 4$ s for all 5 of these cases and for all the following statistical analyses.

4.2.3 Statistical Analysis of the Catalyst Volume Fraction

The normalized axial mean of α_s, $\varepsilon(r)$, shown in Figure 4.6, reveals the difference between the low feed tube flow rate cases (f8, f17, and f33) and the high feed tube flow rate cases (f51 and f68) with a significantly lower $\varepsilon(r)$ along the feed tube wall ($R_T = 0.643$ cm) in the latter two cases due to more gas passing along the tube wall. We note a reversal of slope in $\varepsilon(r)$ vs. r between the two sets of cases, which results in a less dense bed for the lower v_{ft} cases and a more packed bed for the high v_{ft} cases. When plotted against the bed height, the packing of the bed is more evident for f51 and f68 with the latter packing to about 80% the maximum possible packing vs. $\sim 70\%$ for the former. Additionally, we note that the bed height is defined by a sharp drop in $\varepsilon(z)$ vs. z for f8, f17, and f33 while the bed height is less sharply defined for the other two cases, with longer, gradual drops in $\varepsilon(z)$ with increasing

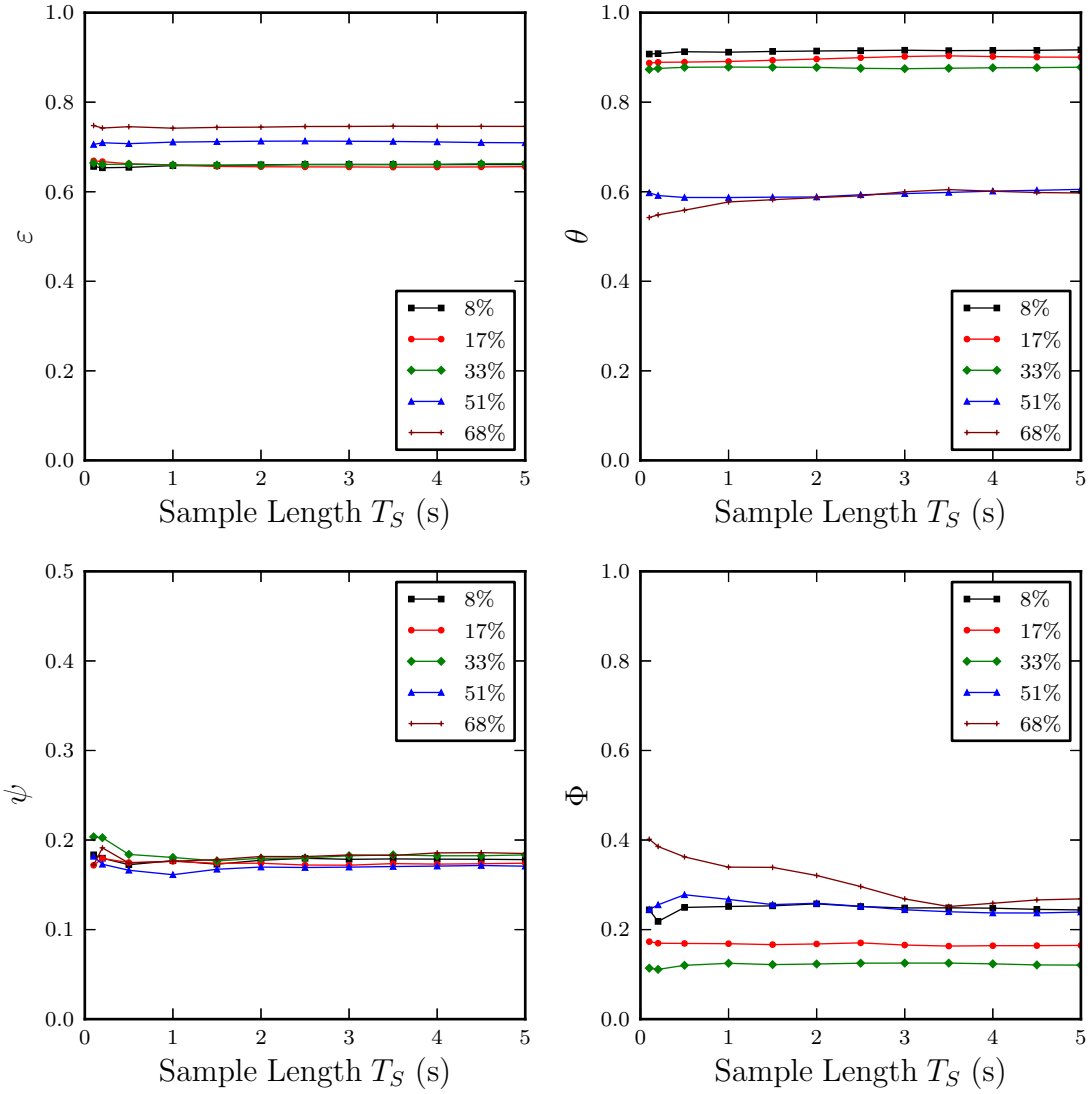

Figure 4.5: Statistical convergence of bed mixing parameters (ε, ψ, θ, and Φ) vs. sampling period (T_S) for simulations run with $Q_{ft}/Q_{total} \approx 8\%$, 17%, 33%, 51%, and 68% with a constant $Q_{total} \approx 55$ cm^3/s, where $\varepsilon = \left\langle \overline{\alpha_s} \right\rangle / \alpha_{s,max}$, $\psi = \left\langle \overline{\alpha_s'^2} \right\rangle / \alpha_{s,max}'^2$, $\theta = \left\langle \overline{\xi(r)} \right\rangle / \xi_{ideal}$, and $\Phi = \left\langle \overline{\xi'^2} \right\rangle / \left\langle \overline{\xi} \right\rangle^2$.

z. This gradualness of slope vs. z indicates a less even bed height for f51 and f68, which can also be noted in the contour plots in Figure 4.4.

Despite the fact that there are more bubbles in the low feed tube flow rate cases, the catalyst variance parameter $\psi(r)$ peaks to a significantly higher value for the high feed tube flow rate cases near the feed tube (see Figure 4.6). The catalyst variance $\psi(z)$ also peaks higher around the top of the catalyst bed for the high feed tube velocity cases. For the three lower v_{ft} cases, we note a nearly linear increase in variance of the catalyst with bed height above the feeding tube ($H_T = 1.558$ cm), which is indicative of bubble growth vs. bed height. Such a linear growth is not seen for the high feed tube flow rate cases due to a general lack of bubbling within the bed. Similar to the sharp drop in $\varepsilon(z)$ for the low v_{ft} cases, we note a sharp drop in $\psi(z)$ at the top of the catalyst bed and, in f51 and f68, wide trailing edges of the peaks in variance. We again attribute these responses to the spouting of particles along the feed tube wall above the catalyst bed, which cause variations in the bed height across the radius of the bed.

The occurrence of the trough in $\varepsilon(R_T)$ and the peak in $\psi(R_T)$ for the high v_{ft} cases can be linked to the direction of flow along the feed tube wall, which reverses from negative to positive when $Q_{ft}/Q_{total} > 33\%$. The fluidizing velocity, and particularly how close it is to v_{mb}, is one of the main differences between cases run above and cases run below $Q_{ft}/Q_{total} = 33\%$. The three cases run at $Q_{ft}/Q_{total} \approx 8\%$, 17%, and 33% have respective fluidization velocities of $v_{fl} = 2.55$, 2.27, and 1.83 cm/s, which are well above $v_{mb} \approx 0.9$ cm/s. Meanwhile, the other two cases, where $Q_{ft}/Q_{total} \approx 51\%$ and 69%, respectively have $v_{fl} = 1.33$ and 0.86 cm/s, much closer to v_{mb}. Although $v_{fl} = 0.9$ cm/s is the first velocity associated with bubble formation, $v_{fl} = 1.5$ cm/s was the lowest fluidizing velocity at which both the bed catalyst variance ψ and the percentage of the bed occupied by the bubble phase

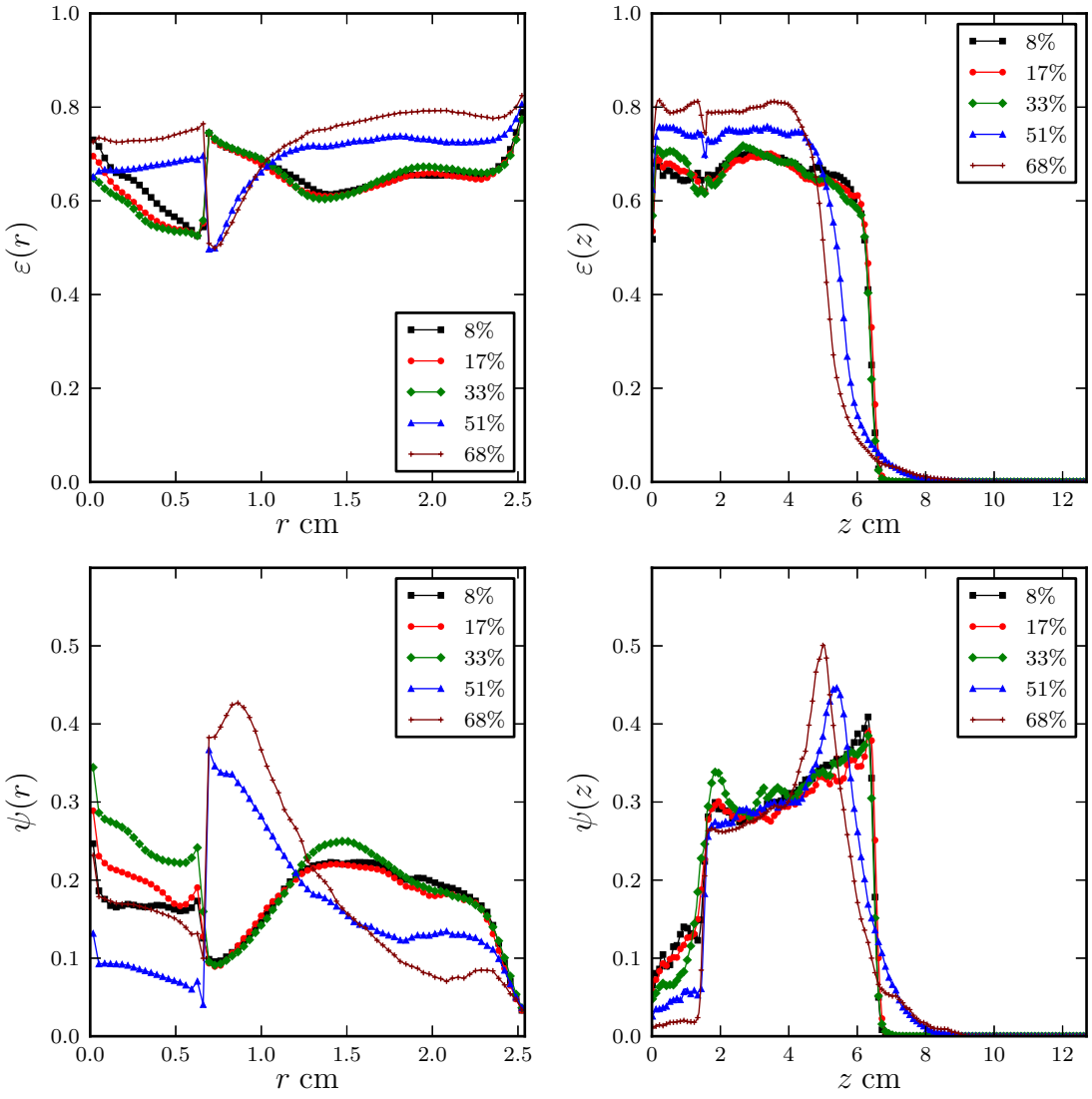

Figure 4.6: The effect of the gas distribution between the fluidizer and the feed tube (Q_{ft}/Q_{total} (8%, 17%, 33%, 51%, and 68%; $Q_{total} \approx 55$ cm^3/s) on the mixing of the catalyst. Axial (left) and radial (right) time-ensemble means (top) and variances (bottom) of the solids volume fraction from Fluent simulations with a feed tube: $\varepsilon(r) = \left\langle \overline{\alpha_s(r)} \right\rangle / \alpha_{s,max}$, $\varepsilon(z) = \left\langle \overline{\alpha_s(z)} \right\rangle / \alpha_{s,max}$, $\psi(r) = \left\langle \overline{\alpha_s'^2(r)} \right\rangle / \alpha'^2_{s,max}$, and $\psi(z) = \left\langle \overline{\alpha_s'^2(z)} \right\rangle / \alpha'^2_{s,max}$.

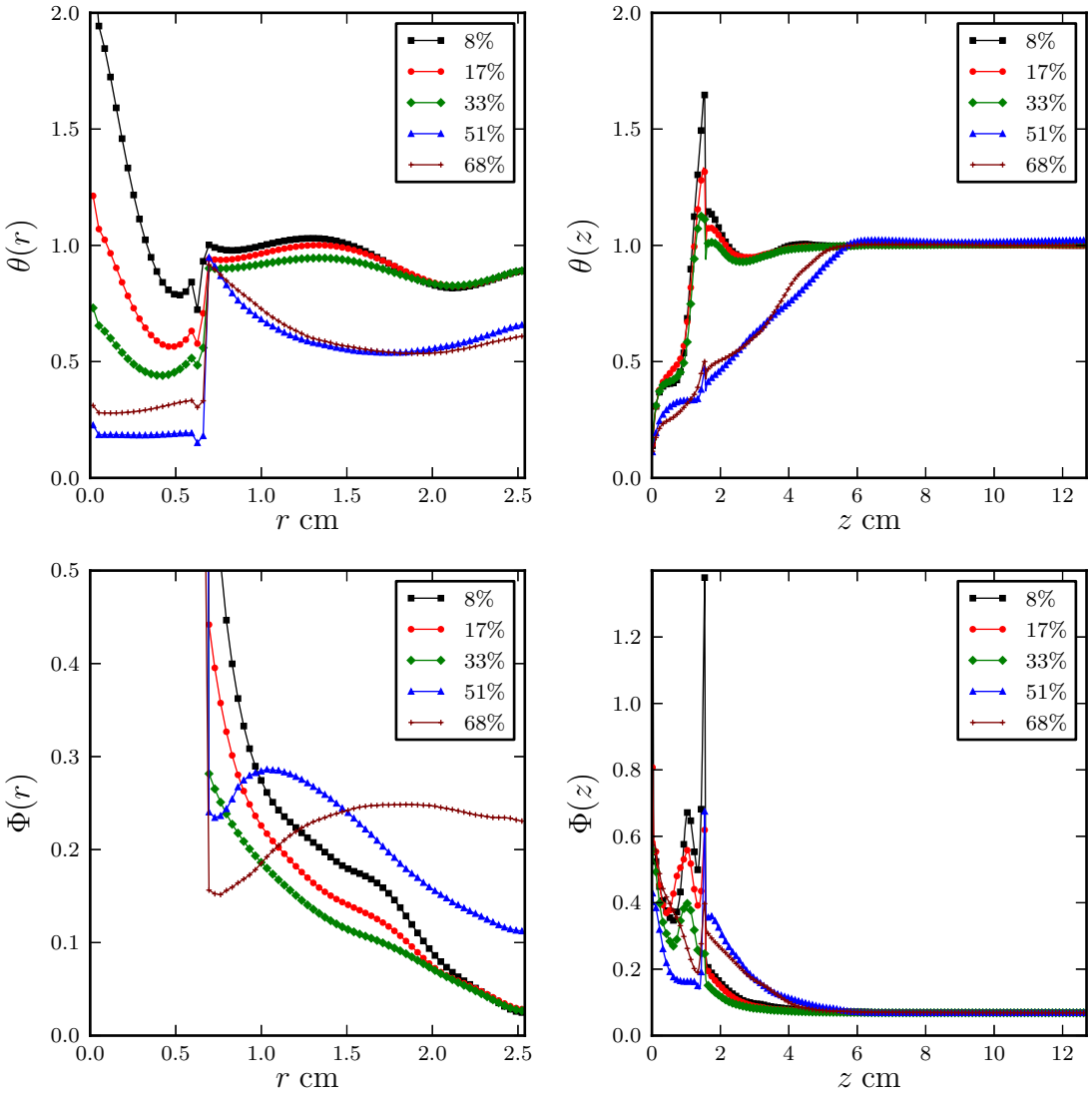

Figure 4.7: The effect of the gas distribution between the fluidizer and the feed tube (Q_{ft}/Q_{total} (8%, 17%, 33%, 51%, and 68%; $Q_{total} \approx 55$ cm^3/s) on the mixing of the feed tube tracer gas. Axial (left) and radial (right) time-ensemble means (top) and variances (bottom) of the mixture fraction from Fluent simulations with a feed tube: $\theta(r) = \left\langle \overline{\xi(r)} \right\rangle / \xi_{ideal}$, $\theta(z) = \left\langle \overline{\xi(z)} \right\rangle / \xi_{ideal}$, $\Phi(r) = \left\langle \overline{\xi'^2(r)} \right\rangle / \left\langle \overline{\xi(r)} \right\rangle^2$, and $\Phi(z) = \left\langle \overline{\xi'^2(z)} \right\rangle / \left\langle \overline{\xi(z)} \right\rangle^2$.

χ were significantly high (see Figure 4.3). Thus, the two high v_{ft} cases have a v_{fl} less than the significant bubbling velocity (1.5 cm/s).

4.2.4 Statistical Analysis of the Mixture Fraction

The mixing of the catalyst does not directly show how the feeding tube gas mixes within the bed. Rather, we look at the mixture fraction statistics. Within the majority of the bed, we note from Figure 4.7 that $\theta(r)$ and $\theta(z)$ are close to unity (nearly ideally mixed) for f8, f17, and f33. The cases f51 and f68 do not show as good of mixing except near the feeding tube. These high v_{ft} cases show a linear increase in mixing ($\theta(z)$) with bed height rather than a well-mixed case throughout the whole bed.

The variance of the mixture fraction over the squared mean of the mixture fraction vs. radius ($\Phi(r)$) and vs. bed height ($\Phi(z)$) show that the f33 case exhibits the lowest values of $\Phi(r)$ and $\Phi(z)$. Thus, this case has the best mixing of the feed tube gas with the catalyst bed. This is in strong agreement with experimental highest aromatic yield case (when 34% of the total gas flow is injected through the feeding tube). The other four cases show increased variance vs. r and z with f51 and f68 having the worst mixing of the feed tube tracer gas.

4.2.5 Bed Statistics

The mixing parameters (ε, ψ, θ, and Φ) described in Section 3.7.3 are plotted in Figure 4.8. First, we note that ε is nearly constant for the three low v_{ft} cases (f8, f18, and f33) and increases slightly for the other two cases (f51 and f68). The bed variance of the catalyst additionally is similar for all five cases at $\psi \approx 0.18$. Again, we analyze the mixture fraction to determine the mixture quality and compare to the product yields. The bed mean of the mixture fraction over the ideal mixture fraction is close to unity for the lower three v_{ft} cases. For the two higher v_{ft} cases, θ is far from ideal and closer to 0.7 and 0.6.

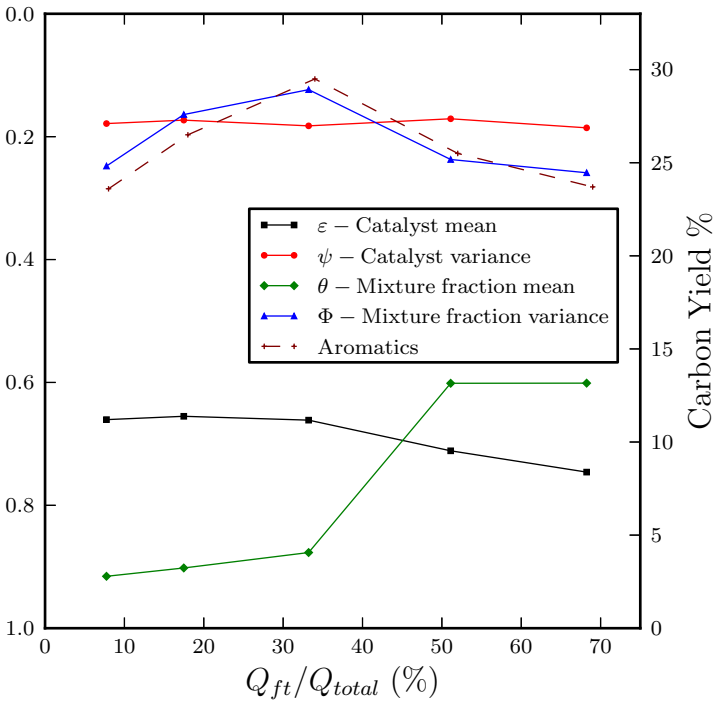

Figure 4.8: Bed catalyst mean and variance, bed mixture fraction mean and variance (left axis, solid lines), and aromatic product yield (left axis, dashed line) vs. the ratio of gas distribution in the feed tube (Q_{ft}/Q_{total}) with a constant $Q_{total} \approx 55$ cm^3/s, where $\varepsilon = \left\langle \overline{\alpha_s} \right\rangle / \alpha_{s,max}$, $\psi = \left\langle \overline{\alpha_s'^2} \right\rangle / \alpha_{s,max}'^2$, $\theta = \left\langle \overline{\xi} \right\rangle / \xi_{ideal}$, and $\Phi = \left\langle \overline{\xi'^2} \right\rangle / \left\langle \overline{\xi} \right\rangle^2$.

The mixture fraction variance over the mean mixture fraction squared Φ within the catalyst bed is minimized at f33, which has the same ratio of Q_{ft}/Q_{total} that a maximum of the aromatic yield was found experimentally ($Q_{ft}/Q_{total} = 34\%$). Similarly, cases above and below the $Q_{ft}/Q_{total} = 34\%$ point agree with the experimental data: the further the case is from this optimum operating condition, the greater the drop in mixing quality (drop in aromatic yield). The value of Φ is close to 2 times higher for the worst mixed case ($\Phi \approx 0.3$ for the 68% case) than for the ideally mixed case ($\Phi \approx 0.15$ for the 33% case).

4.3 Effect of Total Gas Flow Rate

The second set of simulations tests the effect of increasing the total flow rate ($Q_{total}/Q_{mf} \approx$ 3, 4, 6, and 8; $Q_{mf} = 6.917$ cm^3/s) while keeping a constant ratio of the feed tube gas flow rate to the total inflow gas flow ($Q_{ft}/Q_{total} = 33.21\%$). In this section, mixing parameter definitions are excluded from figure captions as these can be found in prior figures, sections, and the List of Symbols. A summary of simulations run can be found in Tables 3.3 and 4.2.

4.3.1 Visualization

As in Section 4.2.1, time snapshots of α_s, Y_{Ar}, and v_s are shown after the tracer gas mass fraction at the outlet is roughly constant (see Figure 4.9). From Figure 4.9a, we note that at low total flow rate $Q_{total}/Q_{mf} \approx 3$ and 4 (hereafter t3 and t4, respectively), there is a lack of bubbling within the majority of the bed while bubbling is evident at the higher two total flow rates, $Q_{total}/Q_{mf} \approx 6$ and 8 (hereafter t6 and t8, respectively). For t3 and t4, $v_{fl} = 0.72$ and 0.96 cm/s, respectively, and for t6 and t8, $v_{fl} = 1.44$ and 1.92 cm/s, respectively. Thus, the lack of bubbling within the bed is consistent with the lack of significant bubbling below $v_{fl} = 1.5$ cm/s. The tracer gas from the feeding tube shows a lack of mixing within the majority of the bed for t3 and t4 as the gas rises from the feeding tube and passes quickly through the system along the feeding tube outer wall. The t6 and t8 cases demonstrate that the Ar tracer gas disperses radially before proceeding out of the bed.

Case abbr.	$\frac{Q_{total}}{Q_{mf}}$	Q_{total} $\left(\frac{\text{cm}^3}{\text{s}}\right)$	$\frac{Q_{ft}}{Q_{total}}$ (%)	v_{ft} $\left(\frac{\text{cm}}{\text{s}}\right)$	v_{fl} $\left(\frac{\text{cm}}{\text{s}}\right)$
t3	3.15	21.82	33.21	5.57	0.72
t4	4.21	29.09	33.21	7.43	0.96
t6	6.31	43.63	33.21	11.14	1.44
t8	8.41	58.18	33.21	14.85	1.92

Table 4.2: Flow rate configurations and abbreviations for simulations with a constant Q_{ft}/Q_{total} as a function of Q_{total}.

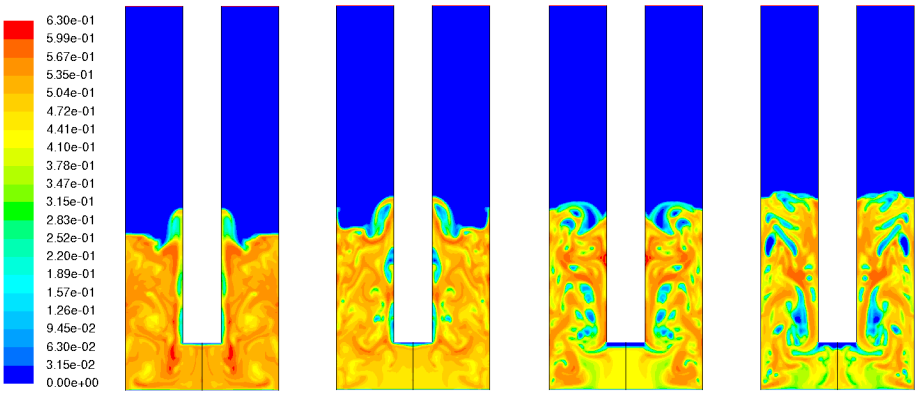

(a) α_s

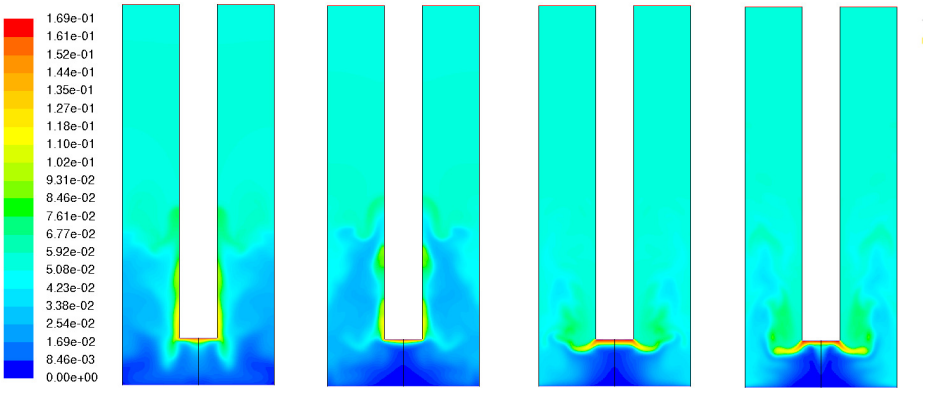

(b) Y_{Ar}

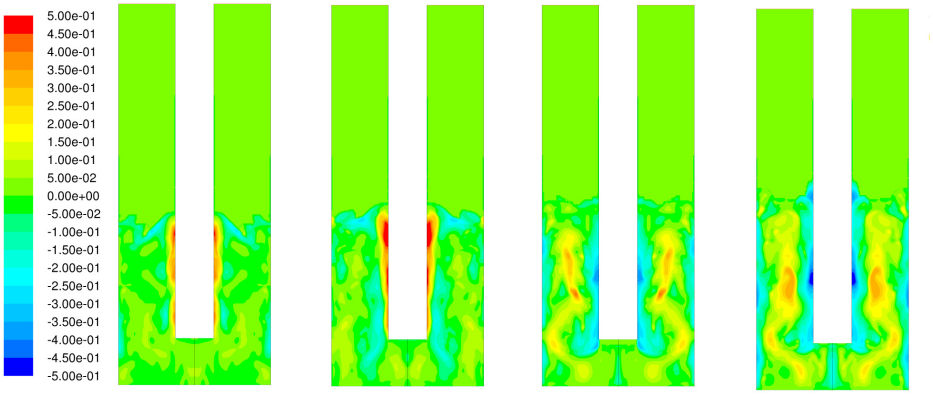

(c) v_s

Figure 4.9: Time snapshots of contour plots of (a) the catalyst volume fraction α_s, (b) the feed tube tracer gas mass fraction Y_{Ar}, and (c) the catalyst axial velocity magnitude v_s for Fluent simulations with a feed tube with a constant $Q_{ft}/Q_{total} \approx 33\%$ and different ratios of Q_{total}/Q_{mf}: (left-to-right: 3, 4, 6, and 8).

The axial velocity component of the catalyst in Figure 4.9c reveals that for t3 and t4, the catalyst rises quickly along the feeding tube. There is a marked shift in the higher total flow rate cases with downflow of the catalyst along the feeding tube and a higher upward flow in between the feeding tube and the reactor wall. This is very similar to the behavior noted in the first set of simulations, and it can be noted that in both sets of simulations, the change in flow occurs when v_{fl} transitions from below ~ 1.5 cm/s to above ~ 1.5 cm/s, the so-called significant bubbling velocity.

4.3.2 Statistical Convergence

As with the first set of simulations, we ensure that statistical convergence of the set of mixing parameters $\{\varepsilon, \psi, \theta, \Phi\}$ has been achieved before performing further statistics. The sampling time period of statistical convergence T_S is determined from Figure 4.10. All four statistical quantities converge after about 4 s. The variance of the mixture fraction statistic Φ fluctuates around the converged value for t3 and t4, but these fluctuations have relatively small oscillations. Regardless of any small-scale variations, after 4 s, all the statistics pertaining to the four different cases maintain the same qualitative behavior with varying flow rates. We thus again establish the same $T_S = 4$ s as was used for the first set of simulations.

4.3.3 Statistical Analysis of the Catalyst Volume Fraction

Plotted in Figure 4.11 are the catalyst volume fraction statistics as functions of radius ($\xi(r)$) and of bed height ($\xi(z)$). The first of the plots reveals the difference between the two lower total flow rate cases (t3 and t4) and the two higher total flow rate cases (t6 and t8). Higher $\varepsilon(r)$ is observed along the tube wall for t3 and t4 due to the gas bypassing along the tube wall. The inverse slope of the catalyst volume fraction vs. radius for t6 and t8 shows a marked difference in catalyst distribution. Ultimately, t6 and t8 have a higher void fraction

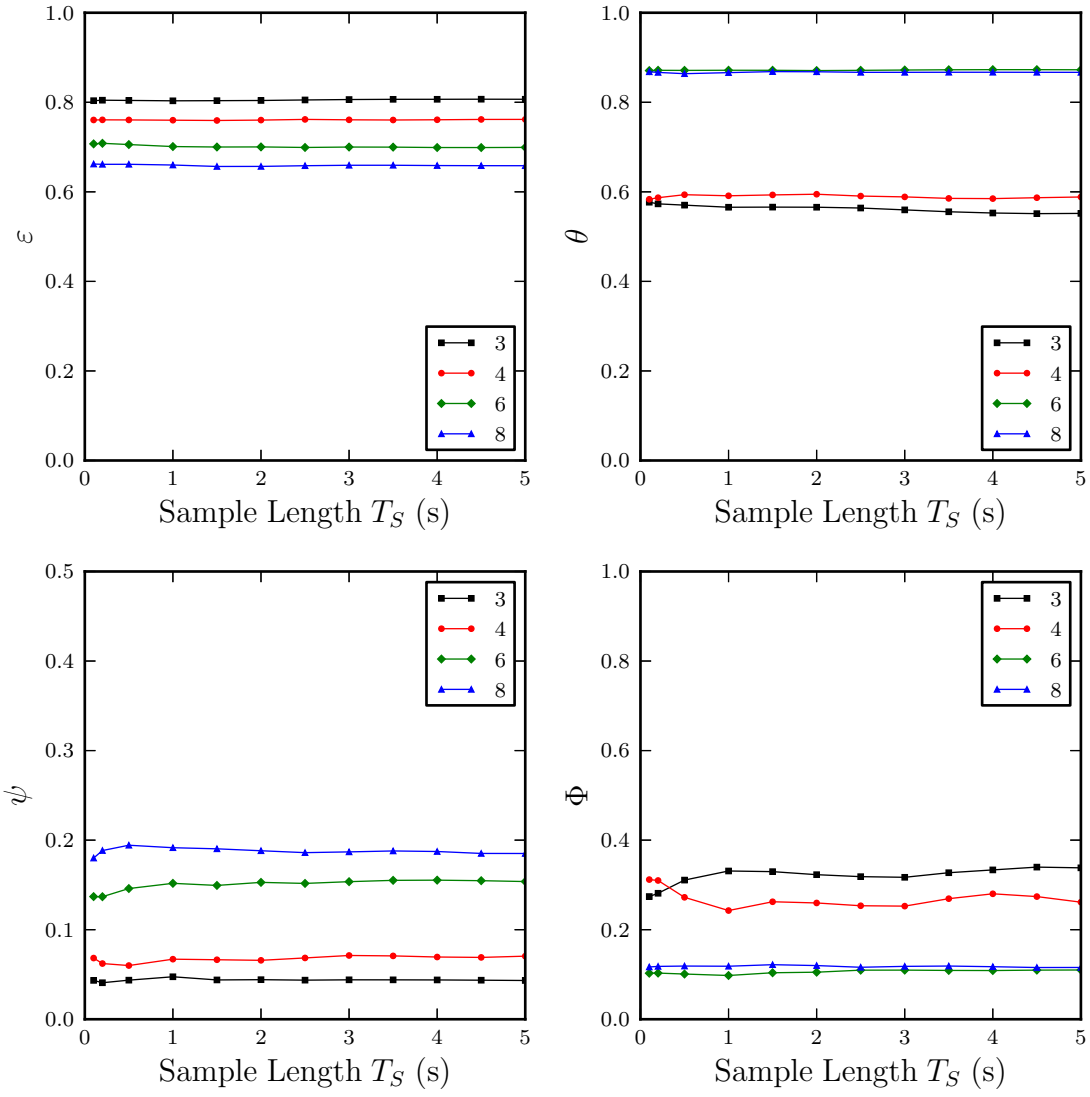

Figure 4.10: Statistical convergence of bed mixing parameters (ε, ψ, θ, and Φ) vs. sampling period (T_S) for simulations run with $Q_{total}/Q_{mf} \approx 3$, 4, 6, and 8 with a constant $Q_{ft}/Q_{total} \approx 33\%$.

within the majority of the bed, as is also to be expected with a higher fluidizing velocity. The high void fraction with high Q_{total} is also evident in the second plot, wherein the bed height increases with Q_{total}.

The catalyst variance parameter $\psi(r)$ is highest along the feed tube wall due to large bubbles passing along the tube for t3 and t4. The lack of internal bubbling causes these cases to have a lower catalyst variance across the majority of the bed than for t6 and t8. The bed height is characterized by a high catalyst variance, as demonstrated by $\psi(z)$ in Figure 4.11. From the width of the trailing edge of this peak, we can again ascertain whether or not the bed height is flat in time and whether particles are blown off the top leading to uneven bed heights. This trailing edge is elongated for t3 and t4 while it is a steep drop for t6 and t8. The contour plots of α_s in Figure 4.11 confirm the same uneven bed height behavior with the particles blown high above the height of the bed along the feeding tube wall for t3 and t4 and a more even dispersion spread across the radius of the bed in the other two cases.

4.3.4 Statistical Analysis of the Mixture Fraction

Figure 4.12 shows that for t6 and t8, $\theta(r)$ is close to unity across the radius of the bed after the feed tube. For t3 and t4, however, the feeding tube tracer gas does not disperse well radially into the bed with $\theta(r) \approx 0.5{-}0.7$. For t3 and t4, $\theta(z)$ increases with bed height, only reaching ideal mixing above the catalyst bed ($\sim 5{-}6$ cm). The t6 and t8 case have $\theta(z > H_T) \approx 1$. For $z < H_T$, the feeding tube tracer gas is poorly mixed for all cases since it must reach deep into the bed and against the flow of the fluidizing gas in order to mix with this portion of the bed.

The mixture fraction variance parameter $\Phi(r)$ is high when $r \leq R_T$ for t6 and t8. We focus mostly on the variance across the radius in the majority of the bed ($r > R_T$), wherein $\Phi(r)$ decreases steadily for these two cases (see Figure 4.12). This is indicative of better mixing away from the feeding tube wall. We also note a higher $\Phi(r)$ for t3 and t4 with a

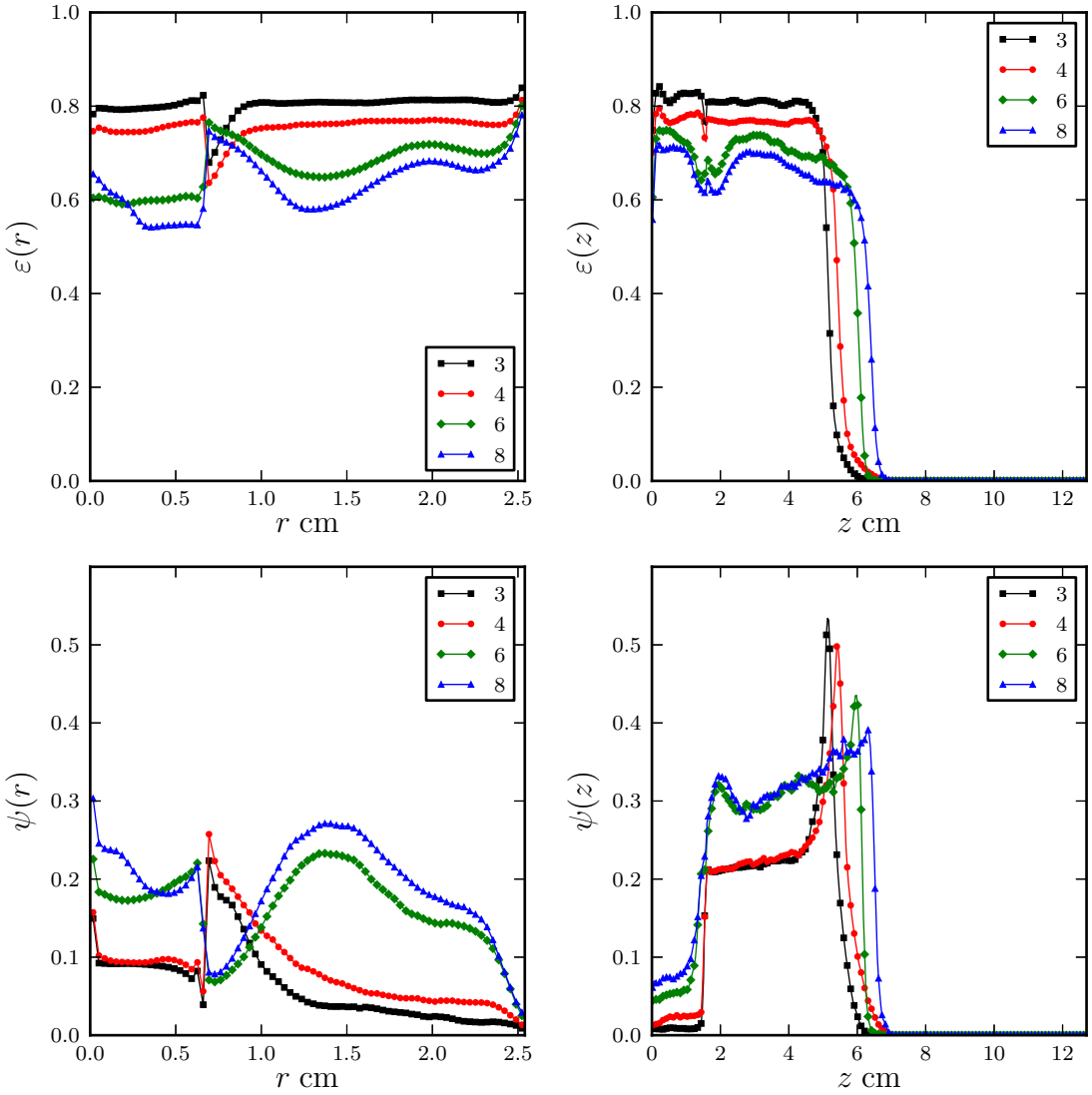

Figure 4.11: The effect of increasing the total gas flow rate ($Q_{total}/Q_{mf} \approx 3$, 4, 6, and 8; $Q_{ft}/Q_{total} \approx 33\%$) on the mixing of the catalyst. Axial (left) and radial (right) time-ensemble mean (top) and variance (bottom) of the solids volume fraction from Fluent simulations with a feed tube.

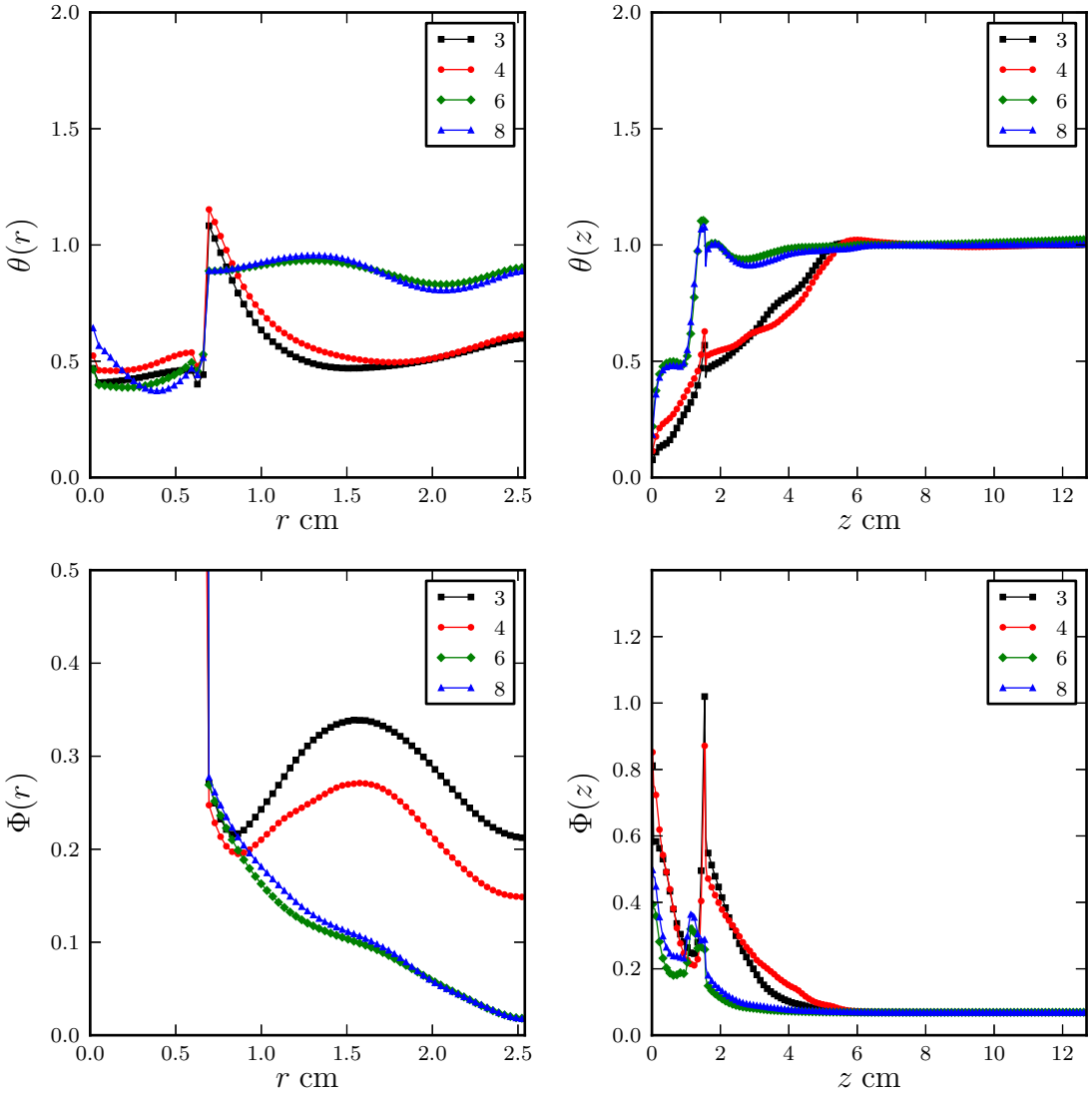

Figure 4.12: The effect of increasing the total gas flow rate ($Q_{total}/Q_{mf} \approx 3$, 4, 6, and 8; $Q_{ft}/Q_{total} \approx 33\%$) on the mixing of the feed tube tracer gas. Axial (left) and radial (right) time-ensemble mean (top) and variance (bottom) of the mixture fraction from Fluent simulations with a feed tube.

peak of variance in between the feed tube wall and the outer wall. For all four cases, above the feeding tube inlet, $\Phi(z)$ decreases with height, and it is significantly lower for t6 and t8 than for the other two cases. The high peaks of $\Phi(z)$ for t3 and t4 can be explained by the fact that the Ar tracer gas is not mixing radially across the bed.

4.3.5 Bed Statistics

Figure 4.13 compares the statistical quantities ε, ψ, θ, and Φ to the aromatics yield percentages. We observe that with increasing total flow rate, ε steadily decreases while ψ increases. This finding simply serves to confirm that by increasing Q_{total}, the bed becomes less dense and the bubbling more vigorous.

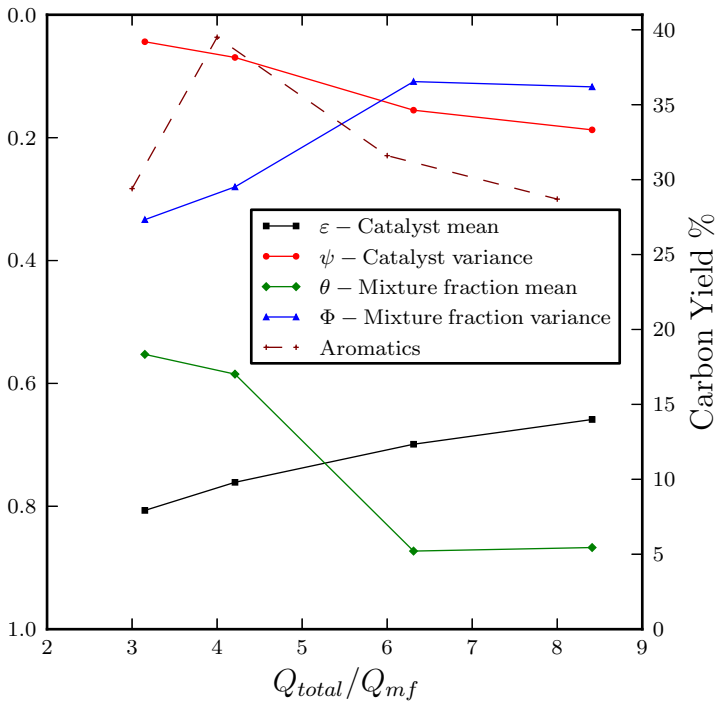

Figure 4.13: Bed mean and variance (solid lines) with aromatic yield (dotted lines) as a function of Q_{total}/Q_{mf}

The mixture fraction is significantly closer to the ideally mixed case for t6 and t8 than for t3 and t4: $\theta \approx 0.9$ for t6 and t8 and $\theta \approx 0.55$ for t3 and t4. By analyzing Φ, we note that the feed tube tracer gas is increasingly better mixed as the flow rate increases, up to $Q_{total}/Q_{mf} \approx 6$, where a slight minimum of Φ is found. The high variance in the low total flow rate cases can be traced back to the feeding tube gas rising along the feeding tube outer wall, which causes a large volume of the gas to bypass the majority of the bed. The shallow minimum of the mixture fraction variance over the mean-squared at t6 is not a complete match with the significant peak in aromatic yield, noted at $Q_{total}/Q_{mf} \approx 4$. Although the CFD simulations do not exhibit the same exact point of best mixing as the experimental reactor, the simulations do still show a subtle, best-mixed case vs. Q_{total} at $v_{fl} \approx 1.5$ cm/s, the point of significant internal bubbling. This shows that the bubbling point is a critical point for mixing within the fluidized bed.

CHAPTER 5

CONCLUSIONS

Computational fluid dynamics (CFD) simulations run on ANSYS© Fluent were used to simulate a three-phase fluidized bed reactor (FBR). As in a traditional FBR, the bed is fluidized by a gas stream entering through the bottom of the reactor. An additional gas stream enters downward through a vertical tube in the center of the reactor. The overarching objective is to optimize the mixing of this second gas stream with the particles in the bed. The simulations are validated using experimental data and theory for the traditional two-phase configuration. Good agreement was found with the minimum fluidization velocity and it was noted that in the simulations, bubbling within the bed did not occur until a fluidizing velocity of 0.9 cm/s, the minimum bubbling velocity. Significant bubbling did not occur until $v_{fl} = 1.5$ cm/s. Ultimately, the significance of these findings manifested in the simulations run with a feeding tube as it was noted that heavy feeding tube gas bypassing occurred along the feeding tube wall when the fluidizing velocity was below 1.5 cm/s. The feed tube tracer gas dispersed radially into the majority of the bed for cases run with $v_{fl} \gtrsim 1.5$ cm/s. The flow of the gas along the feed tube wall is thus important in determining whether a flow rate configuration will be well-mixed or not. The feed tube disperses radially into the bed only if the bed consists of a more dilute, bubbling bed. This could be the primary explanation for why there is a peak in aromatic yield when adjusting both the fluidizing and the feeding tube velocities simultaneously.

In the first set of simulations in which the feeding tube flow rate is varied with a constant total flow rate, we find very good agreement with the experimental reactor. Here, we find

a minimum of $\Phi = \left\langle \overline{\xi'^2} \right\rangle / \left\langle \bar{\xi} \right\rangle^2$, and thus a maximum of mixing of the feeding tube tracer gas with the catalyst bed, at the same $Q_{ft}/Q_{total} \approx 34\%$ that produced the highest aromatic yield. In the second set of simulations, where Q_{ft}/Q_{total} was held constant and Q_{total} was varied, there is also a minimum in Φ at $Q_{total}/Q_{mf} \approx 6$. This minimum is close to but not at the same $Q_{total}/Q_{mf} = 4$ that a maximum aromatic yield was found experimentally.

It should be noted that the CFD simulations were run with multiple assumptions, including a 2D-axisymmetric assumption, no cellulose or chemical kinetics, and a constant particle diameter (instead of the actual bimodal distribution). Thus, it is not expected that the CFD simulations will fully match the behavior of the experimental fluidized bed. As the fluidized bed with the tube is enclosed and insulated, it is difficult to confirm the fluidization behavior within the bed such as the flow direction along the walls or if internal bubbling occurs. One experimental test could provide validity to the CFD simulations if v_{mb} is noted to be around $1.0-1.5$ cm/s. If this is indeed the case, then, as the simulations show, it is likely that the radial dispersion of the feeding tube gas (and thus the radial dispersion of the gasified cellulose) is best when the internal bed is bubbling.

From the simulations, it was shown that the bed is the most well-mixed in configurations right above the bubbling border. Thus, we conclude, that the highest aromatic yields should occur when both $v_{fl} \geq v_{mb}$ and there is a significant amount of feeding tube flow rate ($Q_{ft}/Q_{total} \approx 34$ % in this case). A further test of this theory would be to determine v_{mb} experimentally, and then to fix v_{fl} to v_{mb} and adjust the feeding tube flow rate, noting the aromatic yields. Based on what we observe in our simulations, v_{mb} can be determined experimentally in the enclosed reactor by analyzing the standard deviation in time of the inlet pressure vs. fluidizing velocity, as was done in Figure 4.1, and noting when the standard deviation increases significantly. Running cases with these flow rate configurations ($v_{fl} \approx$

v_{mb}) and adjusting v_{ft} is our suggestion for both further experimental and further simulation work.

Additional future work to extend from this thesis is running simulations to test how the mixing is affected by the scale-up of the reactor to a full industrial size, running a 3D model simulation in order to verify the 2D-axisymmetric model by comparing the volume-weighted statistics for each, and simulating chemical kinetics. Scale-up, 3D simulations, and chemical reactions provide computational challenges, however, particularly because simulation run times were not significantly improved when run on 32 processors instead of 8 processors. Further tests of the effect of the mesh size and time step size could help alleviate the problem of long run times by using a more coarse mesh or larger time steps.

The computational fluid dynamics simulations of this non-standard fluidized bed provide a challenge in both numerical modeling and computational effort. The simulations operate as both confirmation for the experimental reactor and a stand-alone testing of hydrodynamic mixing within an unconventional biomass reactor feeding mechanism through the use of a central, downward-facing feeding tube. The statistical analyses and methods described and implemented in this thesis can further serve to quantify mixing within fluidized beds of any configuration.

APPENDIX

GOVERNING EQUATIONS AND CLOSURE MODELS

Continuity	
$\frac{\partial \alpha_g}{\partial t} + \nabla \cdot (\alpha_g \boldsymbol{v}_g) = 0$ $\frac{\partial \alpha_s}{\partial t} + \nabla \cdot (\alpha_s \boldsymbol{v}_s) = 0$	[38]
Momentum	
$\rho_g \alpha_g \left(\frac{\partial \boldsymbol{v}_g}{\partial t} + \boldsymbol{v}_g \cdot \nabla \boldsymbol{v}_g \right) = -\alpha_g \nabla P + \nabla \cdot \alpha_g \bar{\bar{\tau}}_g + \alpha_g \rho_g \boldsymbol{g} - \beta(\boldsymbol{v}_g - \boldsymbol{v}_s)$ $\rho_s \alpha_s \left(\frac{\partial \boldsymbol{v}_s}{\partial t} + \boldsymbol{v}_s \cdot \nabla \boldsymbol{v}_s \right) = -\alpha_s \nabla P + \nabla \cdot \bar{\bar{\tau}}_s - \nabla P_s + \alpha_s \rho_s \boldsymbol{s} + \beta(\boldsymbol{v}_g - \boldsymbol{v}_s)$	[38]
Granular Temperature Θ	
$\Theta = \frac{1}{3} \left\langle \boldsymbol{v}_s'^2 \right\rangle$	[52]
Granular Energy	
$\frac{3}{2} \left(\frac{\partial}{\partial t}(\alpha_s \rho_s \Theta) + \nabla \cdot (\alpha_s \rho_s \Theta \boldsymbol{v}_s) \right) = \left(- P_s \bar{\bar{I}} + \bar{\bar{\tau}}_s \right) : \nabla \boldsymbol{v}_s + \nabla \cdot (\kappa_s \nabla \Theta) - \gamma_s - J_s$	[52]
Granular Temperature (Algebraic) Θ	
$\Theta = \frac{-(K_1 \alpha_s + \rho_s) \mathrm{tr}(\bar{\bar{D}}_s)}{2 \alpha_s K_4} + \frac{\sqrt{(K_1 \alpha_s + \rho_s)^2 \mathrm{tr}^2(\bar{\bar{D}}_s) + 4 K_4 \alpha_s [2 K_3 \mathrm{tr}(\bar{\bar{D}}_s^2) + K_2 \mathrm{tr}^2(\bar{\bar{D}}_s)]}}{2 \alpha_s K_4}$	[71]

Table A.1: Governing equations and closure models: I

Granular Temperature Algebraic Abbreviations K_1, K_2, K_3, & K_4

$$
\begin{aligned}
K_1 &= 2(1+e)\rho_s g_0 \\
K_2 &= \frac{4}{3\sqrt{\pi}} d_s \rho_s (1+e)\alpha_s g_0 - \frac{2}{3}K_3 \\
K_3 &= \frac{d_s \rho_s}{2}\left(\frac{\sqrt{\pi}}{3(3-e)}\left[1+\frac{2}{5}(1+e)(3e-1)\alpha_s g_0\right] + \frac{8\alpha_s}{5\sqrt{\pi}} g_0 (1+e)\right) \\
K_4 &= \frac{12(1-e^2)\rho_s g_0}{d_s\sqrt{\pi}}
\end{aligned}
\qquad [71]
$$

Collision Disspipation γ_s

$$
\gamma_s = 12(1-e^2)\frac{\alpha_s^2 \rho_s g_0}{d_s\sqrt{\pi}}\Theta^{\frac{3}{2}} \qquad [52]
$$

Fluctuation Dissipation J_s

$$
J_s = \beta\left(3\Theta - \frac{\beta d_s (\boldsymbol{v}_g - \boldsymbol{v}_s)^2}{4\alpha_s \rho_s \sqrt{\pi\Theta}}\right) \qquad [52]
$$

Solids Pressure P_s

$$
P_s = \alpha_s \rho_s \Theta + 2 g_0 \alpha_s^2 \rho_s \Theta (1+e) \qquad [52]
$$

Solids Bulk Viscosity λ_s

$$
\lambda_s = \frac{4}{3}\alpha_s \rho_s d_s g_0 (1+e)\sqrt{\frac{\Theta}{\pi}} \qquad [52]
$$

Viscous stress tensor of phase k, $\bar{\bar{\tau}}_k$

$$
\begin{aligned}
\bar{\bar{\tau}}_k &= 2\mu_k \bar{\bar{D}}_k + \left(\lambda_k - \frac{2}{3}\mu_k\right)\mathrm{tr}(\bar{\bar{D}}_k)\bar{\bar{I}} \\
\bar{\bar{D}}_k &= \frac{1}{2}[\nabla \boldsymbol{v}_k + (\nabla \boldsymbol{v}_k)^\top]
\end{aligned}
\qquad [75]
$$

Table A.2: Governing equations and closure models: II

Solids Thermal Conductivity κ_s

$$\kappa_s = \frac{2}{(1+e)g_0}\left[1+\frac{6}{5}(1+e)g_0\alpha_s\right]^2\kappa_{dil} + 2\alpha_s^2\rho_s d_s g_0(1+e)\sqrt{\frac{\Theta}{\pi}} \quad [30]$$

$$\kappa_{dil} = \frac{75}{384}\rho_s d_s\sqrt{\pi\Theta}$$

Solids Shear Viscosity μ_s

$$\mu_s = \frac{10\rho_s d_s\sqrt{\Theta\pi}}{96\alpha_s(1+e)g_0}\left[1+\frac{4}{5}g_0\alpha_s(1+e)\right]^2\alpha_s \quad [30]$$

Frictional Viscosity μ_f

$$\mu_f = Fr\frac{(\alpha_s-\alpha_{s,\min})^n}{(\alpha_{s,\max}-\alpha_s)^p}\sin\phi \quad [40]$$

Radial Distribution Model g_0

$$g_0 = \left(1-\frac{\alpha_s}{\alpha_{s,max}}\right)^{-2.5\alpha_{s,max}} \quad [51]$$

Drag Model β

$$\beta = 150\frac{\alpha_s^2\mu_g}{\alpha_g d_s^2} + \frac{7}{4}\frac{\rho_g\alpha_s|\boldsymbol{v}_g-\boldsymbol{v}_s|}{d_s} \quad (\alpha_s \geq 0.2);$$

$$\beta = \frac{3}{4}C_d\frac{\rho_g\alpha_s\alpha_g|\boldsymbol{v}_g-\boldsymbol{v}_s|}{d_s}\alpha_g^{-2.65} \quad (\alpha_s < 0.2) \quad [30]$$

$$C_D = \frac{24}{\mathrm{Re}_s}\left[1+0.15(\mathrm{Re}_s)^{0.687}\right] \quad (\mathrm{Re}_s < 1000);$$

$$C_D = 0.44 \quad (\mathrm{Re}_s \geq 1000)$$

Table A.3: Governing equations and closure models: III

BIBLIOGRAPHY

[1] Abrahamsen, R., and Geldart, D. Behavior of gas-fluidized beds of fine powders. 1. homogeneous expansion. *Powder Technology 26* (1980), 35–46.

[2] Agrawal, K., Loezos, P. N., Syamlal, M., and Sundaresan, S. The role of meso-scale structures in rapid gas-solid flows. *Journal of Fluid Mechanics 445* (2001), 151–185.

[3] ANSYS, Inc. *ANSYS FLUENT 12.0 Theory Guide*, 2009.

[4] ANSYS, Inc. *ANSYS FLUENT 12.0 User's Guide*, 2009.

[5] Asegehegn, T. W., Schreiber, M., and Krautz, H. J. Numerical simulation and experimental validation of bubble behavior in 2D gas-solid fluidized beds with immersed horizontal tubes. *Chemical Engineering Science 66*, 21 (2011).

[6] Baeyens, J. *Heat transfer in gas fluidized beds*. PhD thesis, University of Bradford, 1973.

[7] Bauer, W., and Werther, J. The role of gas-distribution in fluidized-bed chemical reactor design. *Chemical Engineering Communications* (1982).

[8] Bilger, R. W. Turbulent flows with nonpremixed reactants. In *Turbulent reacting flows*. Springer, 1980, pp. 65–113.

[9] Boemer, A., Qi, H., Renz, U., Vasquez, S., and Boysan, F. Eulerian computation of fluidized bed hydrodynamics—a comparison of physical models. In *Proceedings of the 20th International Conference on Fluidized Bed Combustion* (1995).

[10] Bokkers, G. A., van Sint Annaland, M., and Kuipers, J. A. M. Mixing and segregation in a bidisperse gas-solid fluidised bed: a numerical and experimental study. *Powder Technology 140* (2004), 176–186.

[11] Bonilla, C. F., Brooks, R. D., and Walker, Jr., P. L. The viscosity of steam and nitrogen at atmospheric pressure and high temperatures. In *Proceedings of General Discussion on Heat Transfer* (1951).

[12] Broadhurst, T. E., and Becker, H. A. Onset of fluidization and slugging in beds of uniform particles. *American Institute of Chemical Engineers Journal 21* (1975), 238–247.

[13] Chapman, S., and Cowling, T. S. *The mathematical theory of non-uniform gases.* Cambridge University Press, 1970.

[14] Chu, K. W., and Yu, A. B. Numerical simulation of complex particle-fluid flows. *Powder Technology 179* (2008), 104–114.

[15] Chung, T. J. *Computational Fluid Dynamics.* Cambridge University Press, 2002.

[16] Coronella, C. J., Yee, S. Y., and Seader, J. D. Minimum slugging velocity in fluidized beds containing vertical rods. *Fuel 73*, 9 (1993), 1537–1543.

[17] Coulomb, C. A. Essai sur une application des régles de maximis et minimis á quelques problémes de statique, relatifs á l'architecture. *Mémoires de Mathématique & de Physique présentés á l'Académie Royale des Sciences par divers Savans, & lûs dans ses Assemblées 7* (1776), 343–382.

[18] Crowe, C., Sommerfeld, M., and Tsuji, Y. *Multiphase Flows with Droplets and Particles.* CRC Press, 1998.

[19] Das Sharma, S., Pugsley, T., and Delatour, R. Three-dimensional CFD model of the deaeration rate of FCC particles. *American Institute of Chemical Engineers Journal 52* (2006), 2391–2400.

[20] Davidson, J. F., Clift, R., and Harrison, D., Eds. *Fluidization*, 2nd ed. Academic Press, 1985.

[21] Davies, L., and Richardson, J. F. Gas interchange between bubbles and the continuous phase in a fluidised bed. *Transactions of the Institution of Chemical Engineers 44* (1966), T293–T305.

[22] Deen, N. G., van Sint Annaland, M., van der Hoef, M. A., and Kuipers, J. A. M. Review of discrete particle modeling of fluidized beds. *Chemical Engineering Science 62* (2007), 28–44.

[23] Di Renzo, A., and Di Maio, F. P. Homogeneous and bubbling fluidization regimes in DEM-CFD simulations: hydrodynamic stability of gas and liquid fluidized beds. *Chemical Engineering Science 62* (2007), 116–130.

[24] Enwald, H., Peirano, E., and Almstedt, A. E. Eulerian two-phase flow theory applied to fluidization. *International Journal of Multiphase Flow 22* (1996), 21.

[25] Ergun, S. Fluid flow through packed columns. *Chemical Engineering Progress 48*, 2 (1952), 89–94.

[26] Ferschneider, G., and Mege, P. Eulerian simulation of dense phase fluidized beds. *Rev. Inst. Fr. Pet. 51*, 2 (1996), 301–307.

[27] Frantz, J. S. Minimum fluidization velocities and pressure drop in fluidized beds. *Chemical Engineering Progress Symposium Series 62* (1966), 21–31.

[28] Gao, J., Chang, J., Xu, C., Lan, X., and Yang, Y. CFD simulations of gas solid flow in FCC strippers. *Chemical Engineering Science 63* (2008), 1827–1841.

[29] Geldart, D. Types of gas fluidization. *Powder Technology 7* (1973), 285–292.

[30] Gidaspow, D. *Multiphase flow and fluidization.* Academic Press, San Diego, 1994.

[31] Hong, R. Y., Li, H. Z., Li, H. B., and Wang, Y. Studies on the inclined jet penetration length in a gas-solid fluidized bed. *Powder Technology 92*, 3 (1997), 205–212.

[32] Hoomans, B. P. B., Kuipers, J. A. M., Briels, W. J., and Van Swaaij, W. P. M. Discrete particle simulation of bubble and slug formation in a two-dimensional gas-fluidized bed: a hard sphere approach. *Chemical Engineering Science 51*, 1 (1996), 99–118.

[33] Hosseini, S. H., Rahimi, R., Zivdar, M., , and Samimi, A. CFD simulation of gas-solid bubbling fluidized bed containing FCC particles. *Korean Journal Chemical Engineering 26*, 5 (2009), 1405–1413.

[34] Hosseini, S. H., Zhong, W., Esfahany, M. N., Pourjafar, L., and Azizi, S. CFD simulation of the bubbling and slugging gas-solid fluidized beds. *Journal of Fluids Engineering 132*, 4 (2010).

[35] Hull, A. S., Chen, Z., and Agarwal, P. K. Influence of horizontal tube banks on the behavior of bubbling fluidized beds: 1. bubble hydrodynamics. *Powder Technology 103* (1999), 230–242.

[36] Hull, A. S., Chen, Z., and Agarwal, P. K. Influence of horizontal tube banks on the behavior of bubbling fluidized beds: 2. mixing of solids. *Powder Technology 111* (2000), 192–199.

[37] Ishii, M. *Thermo-Fluid Dynamic Theory of Two-Phase Flow.* Direction des Etudes et Recherches d'Electricitò de France. Eyrolles, 1975.

[38] Jackson, R. Locally averaged equations of motion for a mixture of identical spherical particles and a newtonian fluid. *Chemical Engineering Science 52* (1997), 2457.

[39] Jenkins, J. T., and Savage, S. B. A theory for the rapid flow of identical smooth, nearly elastic spherical particles. *Journal of Fluid Mechanics 130* (1983), 187–202.

[40] Johnson, P. C., and Jackson, R. Frictional collisional constitutive relations for antigranulocytes-materials, with application to plane shearing. *Journal of Fluid Mechanics 176* (1987), 67–93.

[41] Karanjkar, P., Coolman, R. J., Blatnik, M. T., Almalkie, S., de Bruyn Kops, S. M., Mountziaris, T. J., Conner, W. C., and Huber, G. W. Hydrodynamics of a fluidized bed reactor for catalytic fast pyrolysis of cellulose to make green aromatics. In preparation, 2013.

[42] Kestin, J., Ro, S. T., and Wakeham, W. A. Viscosity of noble gases in the temperature range 25-700^{o}C. *The Journal of Chemical Physics 56*, 8 (1972), 4119–4124.

[43] Law, C. L., Tasirin, S. M., Daud, W. R. W., and Geldart, D. Effect of vertical baffles on particle mixing and drying in fluidized beds of group d particles. *China Particuology 1*, 3 (2003), 115–118.

[44] Li, T., Dietiker, J., Zhang, Y., and Shahnam, M. Cartesian grid simulations of bubbling fluidized beds with a horizontal tube bundle. *Chemical Engineering Science 66* (2011), 6220–6231.

[45] Li, T., Pougatch, K., Sacludean, M., and Grecov, D. Mixing of a secondary gas injection in a bubbling fluidized bed. *Chemical Engineering Research and Design 87* (2009), 1451–1465.

[46] Li, T., Pougatch, K., Salcudean, M., and Grecov, D. Numerical simulation of horizontal jet penetration in a three-dimensional fluidized bed. *Powder Technology 184*, 1 (2008), 89–99.

[47] Lindborg, H., and Jakobsen, H. A. Sorption enhanced steam methane reforming process performance and bubbling fluidized bed reactor design by use of a two-fluid model. *Industrial and Engineering Chemistry Research 48* (2009), 1332–1342.

[48] Lindborg, H., Lysberg, M., and Jakobsen, H. A. Practical validation of the two-fluid model applied to dense gas-solid flows in fluidized beds. *Chemical Engineering Science 62* (2007), 5854–5869.

[49] Loezos, P. N., Costamagna, P., and Sundaresan, S. The role of contact stresses and wall friction on fluidization. *Chemical Engineering Science 57* (2002), 5123–5141.

[50] Louge, M. Y., Mastorakos, E., and Jenkins, J. T. The role of particle collisions in pneumatic transport. *Journal of Fluid Mechanics 231*, 8 (1991), 345.

[51] Lun, C. K. K., and Savage, S. B. The effects of an impact velocity dependent coefficient of restitution on stresses developed by sheared granular matrials. *Acta Mechanica 63* (1986), 15–44.

[52] Lun, C. K. K., Savage, S. B., Jeffrey, D. J., and Chepurniy, N. Kinetic theories for granular flow - inelastic particles in couette-flow and slightly inelastic particles in a general flowfield. *Journal of Fluid Mechanics 140* (1984), 223–256.

[53] Mckeen, T., and Pugsley, T. Simulation and experimental validation of a freely bubbling bed of FCC catalyst. *Powder Technology 129* (2003), 139–152.

[54] Merry, J. M. D. Penetration of a horizontal gas jet into a fluidised bed. *Transactions of the Institution of Chemical Engineers and the Chemical Engineer 49*, 4 (1971), 189.

[55] Miller, C. O., and Logwinuk, A. K. Fluidization studies of solid particles. *Engineering and Process Development 43*, 5 (1961), 1220–1226.

[56] Olsson, S. E., Wiman, J., and Almstedt, A. E. Hydrodynamics of a pressurized fluidized bed with horizontal tubes: Influence of pressure, fluidization velocity and tube-bank geometry. *Chemical Engineering Science 50*, 4 (1995), 581–592.

[57] Ozawa, M., Umekawa, H., Furui, S., Hayashi, K., and Takenaka, N. Bubble behavior and void fraction fluctuation in vertical tube banks immersed in a gas-solid fluidized-bed model. *Experimental Thermal and Fluid Science 26* (2002), 643–652.

[58] Papadikis, K., Gu, S., and Bridgwater, A. V. Geometrical optimzation of a fast pyrolosis bubbling fluidized bed reactor using computational fluid dynamics. *Energy Fuels 24* (2010), 5634–5651.

[59] Parmentier, J. F., Simonin, O., and Delsart, O. A numerical study of fluidization behavior of Geldart B, A/B and A particles using eulerian multifluid modeling approach. In *Ninth International Conference on Circulating Fluidized Beds* (2008), J. Werther, K. E. Wirth, and W. Nowak, Eds.

[60] Patil, D. J., Annaland, A. V., and Kuipers, J. A. M. Critical comparison of hydrodynamic models for gas-solid fluidized beds - Part II: freely bubbling gas-solid fluidized beds. *Chemical Engineering Science 60*, 1 (2005), 73–84.

[61] Petersen, H. The properties of helium: density, specific heats, viscosity, and thermal conductivity at pressures from 1 to 100 bar and from room temperature to about 1800 K. Tech. rep., Danish Atomic Energy Commission: Research Establishment Risö, 1970.

[62] Pillai, B. C., and Rao, R. M. Pressure drop & minimum fluidization velocities in air-fluidized beds. *Indian Journal of Technology 9* (1971), 77–86.

[63] Ramamoorthy, S., and Subramanian, N. Axial solids mixing and bubble characteristics in gas-fluidized beds with vertical internals. *The Chemical Engineering Journal 22* (1981), 237–242.

[64] Robinson, C. S. Some factors influencing sedimentation. *Industrial and Engineering Chemistry 18* (1926), 869–871.

[65] Rowe, P. N. Drag forces in a hydraulic model of a fluidized bed: II. *Transactions of the Institution of Chemical Engineers 39* (1961), 175.

[66] Rüdisüli, M., Schildhauer, T. J., Biollaz, S. M. A., and van Ommen, J. R. Bubble characterization in a fluidized bed with vertical tubes. *Industrial & Engineering Chemistry Research 51* (2012), 4748–4758.

[67] Schaeffer, G. Instability in the evolution-equations describing incrompressible antigranulocytes flow. *Journal of Differential Equations 66*, 1 (1987), 19–50.

[68] Song, X. Q., Grace, J. R., Bi, H., Lim, C. J., Chan, E., Knapper, B., and McKnight, C. A. Gas mixing in the reactor section of fluid cokers. *Industrial & Engineering Chemistry Research 44*, 16 (2005), 6067–6074.

[69] Srivastava, A., and Sundaresan, S. Role of wall friction in fluidization and standpipe flow. *Powder Technology 124* (2002), 45–54.

[70] Stokes, G. G. *Mathematical and physical papers.* Cambridge: University Press, 1880.

[71] Syamlal, M., Rogers, W., and J., O'Brien T. *Mfix Documentation Theory Guide.* U.S. Department of Energy, Office of Fossil Energy Technical Note, 1993.

[72] Taghipour, F., Ellis, N., and Wong, C. Experimental and computational study of gas-solid fluidized bed hydrodynamics. *Chemical Engineering Science 60* (2005), 6857–6567.

[73] Tsinontides, S. C., and Jackson, R. The mechanics of gas-fluidized beds with an interval of stable fluidization. *Journal of Fluid Mechanics 255* (1993), 237–274.

[74] van Wachem, B., and Sasic, S. Derivation, simulation and validation of a cohesive particle flow CFD model. *American Institute of Chemical Engineers Journal 54* (2008), 9–19.

[75] van Wachem, B. G. M., Schouten, J. C., van den Bleek, C. M., Krishna, R., and Sinclair, J. L. Comparative analysis of CFD models of dense gas-solid systems. *American Institute of Chemical Engineers Journal 47*, 5 (2001), 1035–1051.

[76] Wang, J., van der Hoef, M. A., and Kuipers, J. A. M. Why the two-fluid model fails to predict the bed expansion characteristics of Geldart A particles in gas-fluidized beds: A tentative answer. *Chemical Engineering Science 64*, 3 (2009), 622–625.

[77] Wang, J., van der Hoef, M. A., and Kuipers, J. A. M. CFD study of the minimum bubbling velocity of Geldart A particles in gas-fluidized beds. *Chemical Engineering Science 65*, 12 (2010), 3772–3785.

[78] Wang, J., Van der Hoef, M. A., and Kuipers, J. A. M. The role of scale resolution versus inter-particle cohesive forces in two-fluid modeling of bubbling fluidization of Geldart A particles. *Chemical Engineering Science 66* (2011), 4229–4240.

[79] Wen, C. Y., and Yu, Y. H. Mechanics of fluidization. *Chemical Engineering Progress Symposium Series 62* (1966), 100.

[80] Wu, Y. Effect of operating temperature on minimum fluidization velocity. *Powder Technology 67*, 2 (1991), 217–220.

[81] Yates, J. G., Ruiz-Martinez, R. S., and Cheesman, D. J. Prediction of bubble size in a fluidized bed containing horizontal tubes. *Chemical Engineering Science 45*, 4 (1990), 1105–1111.

[82] Zhu, H. P., Y., Zhou Z., Yang, R. Y., and Yu, A. B. Discrete particle simulation of particulate systems: A review of major applications and findings. *Chemical Engineering Science 63* (2008), 5728–5770.

[83] Zhu, H. P., and Zhou Z. Y.and Yu, A. B. Discrete particle simulation of particulate systems: Theoretical developments. *Chemical Engineering Science 62* (2007), 3378–3396.

[84] Zimmerman, S., and Taghipour, F. CFD modeling of the hydrodynamics and reaction kinetics of FCC fluidized-bed reactors. *Industrial & Engineering Chemistry Research 44* (2005), 9818–9827.